CONFIDENTIAL

Copy 289
RM L54K04

NACA RM L54K04

NACA

CASE FILE COPY

RESEARCH MEMORANDUM

INVESTIGATION AT MACH NUMBERS OF 1.41, 1.61, AND 1.82 OF TWO VARIABLE-GEOMETRY INLETS HAVING TWO-DIMENSIONAL COMPRESSION SURFACES

By Lowell E. Hasel

Langley Aeronautical Laboratory
Langley Field, Va.

CLASSIFICATION CHANGED TO UNCLASSIFIED
AUTHORITY: NASA PUBLICATION ANNOUNCEMENT NO. 3
EFFECTIVE DATE: DECEMBER 3, 1958

CLASSIFIED DOCUMENT

This material contains information affecting the National Defense of the United States within the meaning of the espionage laws, Title 18, U.S.C., Secs. 793 and 794, the transmission or revelation of which in any manner to an unauthorized person is prohibited by law.

NATIONAL ADVISORY COMMITTEE FOR AERONAUTICS

WASHINGTON

February 23, 1956

CONFIDENTIAL

NATIONAL ADVISORY COMMITTEE FOR AERONAUTICS

RESEARCH MEMORANDUM

INVESTIGATION AT MACH NUMBERS OF 1.41, 1.61, AND 1.82 OF TWO VARIABLE-GEOMETRY INLETS HAVING TWO-DIMENSIONAL COMPRESSION SURFACES

By Lowell E. Hasel

SUMMARY

One-tenth-scale models of two inlet configurations of fighter-type aircraft have been tested in the Langley 4- by 4-foot supersonic pressure tunnel. One model had a nose inlet incorporating a horizontal-ramp compression surface. The second model had a chin-scoop inlet incorporating a vertical splitter. The pressure-recovery and force characteristics of the inlets were determined as a function of mass-flow ratio, angle of inlet compression, angle of attack, and Mach number. An investigation was made of the effects of removing the boundary layer on the compression surfaces by means of area suction.

The maximum pressure recoveries obtained at an angle of attack of 2° at Mach numbers of 1.41, 1.61, and 1.82 from the nose and chin-scoop inlets with solid compression surfaces were 0.95, 0.91, 0.86, and 0.94, 0.91, 0.85, respectively, of the free-stream stagnation pressure. The stable mass-flow range of both inlets was primarily a function of Mach number and decreased from average values of about 0.50 to 0.04 for the nose inlet and from 0.23 to 0.06 for the chin-scoop inlet as the Mach number increased from 1.41 to 1.82. The effects of angle of attack and yaw on pressure recovery of the inlet were consistent with the geometry of the inlets. Increasing the angle of attack had some beneficial effects on the pressure recovery of the nose inlet but little effect on the chin-scoop inlet. Angles of yaw had a detrimental effect on the pressure-recovery and buzz characteristics of the chin-scoop inlet but had little effect on the nose inlet. Elimination of the boundary-layer bleed system on the chin-scoop inlet by means of a fuselage fairing had no effect on the thrust-minus-drag characteristics of the inlet.

The use of area suction on the inlet compression surfaces resulted in maximum pressure recoveries which were 0.02 to 0.06 higher than the recoveries of similar configurations without area suction. In general, the use of area suction did not significantly affect the inlet stability

ranges. Inasmuch as the external-drag increment due to area suction was insignificant, the use of area suction improved the thrust-minus-drag characteristics of both inlets.

INTRODUCTION

An investigation of 1/10-scale models of two inlet configurations of fighter-type aircraft has been made at Mach numbers of 1.41, 1.61, and 1.82 in the Langley 4- by 4-foot supersonic pressure tunnel. One model representing a day fighter had a nose inlet incorporating a horizontal-ramp compression surface. The second model representing an interceptor had a chin-scoop inlet incorporating a vertical splitter. The investigation was conducted to provide experimental pressure-recovery and force data which would assist in establishing a Mach number schedule for the variable-geometry inlets for the aircraft. The investigation included a study of the effects of removing the boundary layer on the compression surfaces by means of area suction. The angles of attack and yaw were varied from 0° to 6° and from 0° to 4°, respectively.

SYMBOLS

A_e duct-exit area, 0.08986 sq ft

A_f model frontal area, 0.2394 sq ft

C_D external drag coefficient, based on model frontal area of 0.2394 sq ft

C_{D_I} internal drag coefficient, based on model frontal area of 0.2394 sq ft

C_L external lift coefficient, based on model frontal area of 0.2394 sq ft

C_m pitching-moment coefficient, based on model frontal area of 0.2394 sq ft and length of 4.065 ft

D drag, lb

H stagnation pressure, lb/sq ft

H_o free-stream stagnation pressure, lb/sq ft

h	height of boundary-layer bleed, in.
M	free-stream Mach number
m	mass flow, slugs/sec
m_o	free-stream mass flow, slugs/sec
p_e	duct-exit static pressure, lb/sq ft
p_o	free-stream static pressure, lb/sq ft
q_o	free-stream dynamic pressure, lb/sq ft
T	engine thrust, lb
T_I	engine thrust at 100-percent pressure recovery, lb
V_e	duct-exit velocity, ft/sec
V_o	free-stream velocity, ft/sec
W	weight of flow of air, lb/sec
y	vertical distance in duct, in.
H/H_o	total pressure recovery at compressor face
H_L/H_o	local total pressure recovery in diffuser
m/m_o	mass-flow ratio, based on inlet capture area of 0.0466 sq ft for inlet A and 0.0511 sq ft for inlet B
α	angle of attack measured from inlet axis, deg
δ	engine-inlet total pressure divided by NACA sea-level pressure
θ	inlet total temperature divided by NACA sea-level temperature
ϕ	angle of compression surface (measured from inlet axis on inlet A), deg
ψ	angle of yaw, deg

TUNNEL

The Langley 4- by 4-foot supersonic pressure tunnel has a single-return closed throat and is capable of operating at Mach numbers from 1.25 to 2.2. The test section employs fixed side walls and flexible top and bottom walls. The nozzle contours are formed by pulling the flexible walls against fixed, but interchangeable, templates. The test-section width is 54 inches. The average test-section heights are 53.3, 53.0, and 58.1 inches at Mach numbers of 1.41, 1.61, and 1.82, respectively. An external source of dry air is provided to maintain a low moisture content in the tunnel so that condensation effects may be avoided. The stagnation pressure can be varied from approximately 0.25 to 2.0 atmospheres.

MODELS

General Description

The two models of this investigation, designated as inlets A and B, were furnished by the aircraft manufacturer. Inlet A represents a day fighter configuration, and inlet B represents an interceptor configuration. A schematic drawing and a photograph of the complete model are shown in figures 1 and 2, respectively. Aerodynamic forces were measured on that part of the inlet forebody forward of station 44.78 (fig. 1(a)). The rearward part of the model (fig. 1(b)) containing the flow nozzle and instrumentation for measuring mass-flow ratio was rigidly attached to the sting support.

Inlet Forebody

General details.- The inlet forebody was separated from the mass-flow measuring assembly by a labyrinth seal with a small clearance gap as illustrated in figure 1(a). An electrical warning system was used to indicate fouling at the gap. The axis of that part of the model forward of station 32.00 was inclined 2° in a positive direction with respect to the sting and balance axis. This inclination facilitated fairing of the inlet external lines into the rearward section of the forebody. The inlet forebody shape behind station 32.00 was identical for both inlets.

Inlet A.- A detailed schematic drawing and a photograph of inlet A are presented in figures 3 and 4, respectively. This configuration has a nose inlet incorporating a gun-sight radar fairing (fig. 4) on the top lip. The plane of the inlet lips was swept 49° from the vertical plane.

Variable geometry was provided by means of removable ramp blocks having compression angles ϕ of 3.0°, 8.0°, and 12.5°. The duct shapes for these ramp angles are shown in figure 3.

Three 12.5° blocks were constructed of porous, sintered surfaces of stainless steel or brass to permit removal of the ramp boundary-layer air. The amount of the ramp surface which was porous was varied during the investigation by progressively filling the porous surface with lacquer. The following table defines the nomenclature used to designate the extent of porous-ramp surface.

Configuration	Location of porous surface in terms of model station (fig. 3)
AB	-2.2 to -0.7
AC	-2.2 to 0.6
AD	-2.2 to 2.4
AE	-2.2 to 4.0

It should be noted that the dimensions -2.2 and 4.0 do not include the short lengths of porous surface on each end which were backed up by a solid surface for fastening purposes. The air passing through the porous surfaces was removed through two exits, one of which is visible in figure 4. These exits were closed during the tests with nonporous ramps.

Four total-pressure tubes were located in the subsonic diffuser at station 7.9 to determine the effect of porous ramps on the diffuser total-pressure distribution.

Inlet B.- A detailed schematic drawing and a photograph of inlet B are presented in figures 5 and 6, respectively. This model had a chin-scoop inlet with a relatively large radome shape forming the nose of the configuration. Inlet B incorporated a vertical splitter for generating the oblique compression shocks. Variable geometry was provided by interchangeable splitter blocks having half-angles ϕ of 3°, 7°, 10°, and 14°. The half-angle of the leading edge of all splitters was 3° (fig. 6). The top view of the inlet (fig. 5) shows that the lip of the inlet was curved considerably.

One 10° half-angle splitter was constructed of porous stainless steel. The extent of the porous surface was varied during the investigation, as on inlet A. The following table defines the nomenclature used to designate the extent of porous-ramp surface.

Configuration	Location of porous surface in terms of model station (fig. 5)
BC	5.8 to 10.6
BD	5.8 to 14.7

As on inlet A, the dimensions 5.8 and 14.7 inches do not include the lengths of porous surface used for support purposes. The air which passed through the porous surfaces escaped from the model by means of the exit shown in figure 5. This exit was closed when not in use.

The splitter of configuration BC was modified, as shown in section BB of figure 5, to provide a 0.007-inch gap between the splitter and the top of the inlet. This gap permitted more of the boundary-layer air to be removed through the porous-splitter air exit.

A total-pressure rake of seven tubes was located in the diffuser (fig. 5) to determine the effect of the porous-splitter surface on the total-pressure distribution.

A boundary-layer bleed system was provided to divert the boundary layer of the fuselage from the inlet. Exits for the bleed system were located on the sides of the fuselage as shown in figures 5 and 6. Bleed heights of 0, 0.15, and 0.21 inch were provided. The intermediate height corresponded to the full-scale configuration. A larger height was provided to account for the variation of height of the boundary layer due to the difference between full-scale and tunnel Reynolds numbers. The bleed height was varied by altering the fuselage fairing ahead of the inlet as shown in figure 5.

Area distribution of ducts.- The area distribution of ducts for both inlets is presented in figure 7. The duct shapes forward of the compressor rake (fig. 1(a)) duplicate the actual airplane installations.

Characteristics of porous materials.- The type of porous surface will be designated by a number (1, 2, or 3) preceding the letter designation used to denote the extent of the porous surface. Materials 1 and 3 were stainless steel and had a relatively rough surface; material 2 was brass and had a smooth, polished surface. The flow characteristics of these materials were obtained by calibrating several of the ramp and splitter configurations. Porosity-characteristics data are presented in figure 8. It should be mentioned that these data were obtained without flow parallel to the surface. The actual flow through the surface is probably less than would be indicated from figure 8 because reference 1 has shown that, for a given pressure difference, the flow through the surface decreases as the flow parallel to the surface increases.

Pressure and force instrumentation.- Pressure-recovery measurements were made at station 32.35, which corresponds to the compressor-face station, by means of four rakes of five total-pressure tubes each. These rakes were spaced at 60° intervals (fig. 1(a), section AA). Two dummy rakes were included to make the installation symmetrical. A set of four total-pressure rakes (fig. 1(a), section BB) of five tubes each were installed at station 48.35 (just ahead of the duct exit) to determine the internal drag. The rakes were spaced at 90° intervals. Static-pressure orifices were also located in the duct walls at station 48.35. Base pressures were measured by means of 12 static-pressure orifices distributed over all the incremental areas making up the base of the inlet forebody. A dynamic-pressure pickup was installed in inlet A at station 7.9 (fig. 3) and in inlet B at station 16.5 (fig. 5) to observe the static-pressure fluctuations in the subsonic diffuser. The forces of the inlet forebody were measured by means of an internal strain-gage balance located as shown in figure 1(a).

Mass-Flow Measuring Assembly

Mass-flow measurements were made by means of the equipment shown in figure 1(b). This installation was designed according to the standards of the American Society of Mechanical Engineers and incorporated damping screens upstream of the flow nozzle. The ratio of nozzle to duct diameters was 0.731. Four static orifices were located at each of the two planes illustrated in figure 1(b). The amount of air passing through the inlet was controlled by means of a butterfly valve located downstream of the flow nozzle.

Faired-Nose Configurations

The faired-nose configurations are shown in figure 9. These configurations were identical with the noses used on other stability models which had no inlets. For comparison, the general outlines of inlets A and B are shown with dashed lines.

TESTS

The tests were conducted at stagnation pressures of 13 pounds per square inch absolute at Mach numbers of 1.41 and 1.61 and at 12 pounds per square inch absolute at a Mach number of 1.82. The corresponding Reynolds numbers per foot of length were 3.7×10^6, 3.7×10^6, and 3.2×10^6. During all the tests the moisture content of the air in the tunnel was maintained at a value low enough to prevent condensation effects in the test section.

The inlets were located upstream of the test-section windows; consequently, the start of buzz could not be determined by observing the air flow around the inlets with a schlieren system. Therefore, the output from the dynamic-pressure pickups, which was fed into an oscilloscope, was used to detect buzz. The start of buzz was considered to occur at the highest mass-flow ratio at which the static-pressure variations were characterized by a low-frequency and a relatively high amplitude fluctuation. For most of the tests, the mass-flow ratio of the buzz transition was easily detected. Oscillograph records of the static-pressure variations which were present just before buzz and after buzz were taken during a large number of the tests; in general, these records verified the visual observations.

The pressures of all models, except those used to calculate mass-flow ratio, were photographically recorded on an inclined multiple-tube manometer board filled with mercury. For these tests the effective specific gravity of the mercury column was about 5.4. The static-pressure difference across the flow nozzle (fig. 1(b)) was measured with a micromanometer filled with Alkazene 42, a fluid which has a specific gravity of about 1.73. The absolute static pressure indicated by the orifices upstream of the nozzle was measured by a mercury micromanometer.

REDUCTION OF DATA

The mass-flow ratio through the inlet m/m_o was calculated as the sum of the mass flows passing through the flow nozzle (fig. 1(b)) and the small gap (fig. 1(a)) at the inlet-forebody base. These mass flows were calculated on the basis of experimental calibrations which were made for both the nozzle and the gap. The difference between the experimental- and the theoretical-calibration curves for the nozzle was about one-half percent. The mass flow through the gap varied from about 2 to 6 percent of the total mass flow passing through the inlet. The mass-flow ratios for inlets A and B are based on inlet-capture areas of 0.0466 and 0.0511 square foot, respectively.

The area-weighted pressure recovery H/H_o was computed from the total pressures measured at the compressor face by assuming that flow symmetry existed about the vertical center line of the duct.

The internal drag coefficient C_{D_I} was calculated from the following equation:

$$C_{D_I} = \frac{m}{q_o A_f}\left[V_o - V_e \cos(\alpha - 2)\right] - \frac{p_e - p_o}{q_o A_f} A_e \cos(\alpha - 2)$$

The model-exit conditions were considered to be the arithmetic average of the measured exit-static and exit-total pressures.

The external-drag-coefficient data C_D were calculated in the usual manner by subtracting the internal and base drags from the indicated balance drag. The lift data have been corrected for the internal lift of the air passing through the inlet by subtracting the term $\frac{mV_e \sin(\alpha - 2)}{q_o A_f}$ from the indicated balance lift. No corrections have been applied to the indicated pitching moments. All force coefficients are based on the frontal area of the model of 0.2394 square foot and a reference length of 4.065 feet.

ACCURACY

Estimates of the absolute accuracy of the drag and pressure-recovery data are difficult to make because of the limited number of pressure tubes which are available to determine the local-flow characteristics. Relative accuracies based on repeatability of data are estimated to be as follows:

H/H_o . . . . . ± 0.01
m/m_o . . . . . ± 0.01
C_D . . . . . ± 0.003

At supercritical conditions the drag errors for certain configurations appear to be larger than ± 0.003. The reasons for these larger discrepancies are not fully understood.

After the data analysis was completed and final figures prepared, information was received from the manufacturer that the initial calibration of the flow nozzle was 1.5 percent in error. Therefore, the mass-flow ratios presented in this report must be reduced by 1.5 percent to obtain the correct values. The maximum error based on a drag coefficient of 0.15 introduced in the drag data is about 3 percent.

PRESENTATION OF RESULTS

The pressure-recovery H/H_o and external-drag C_D data are presented in this report as a function of the mass-flow ratio m/m_o. The maximum range of angle of attack was from 0° to 6°. All angles of attack are referenced to the inlet axis. A dashed-line fairing of the data indicates inlet buzz.

Figure 10 presents data obtained from inlet A with solid ramps for ramp angles ϕ of 3°, 8°, and 12.5°. Only one porous-ramp configuration (1-AE) was tested at all three Mach numbers, and these data are presented in figure 11. The 2° angle-of-attack data from figures 10 and 11 are summarized as a function of ramp angle in figure 12. Included in figure 12 are estimated pressure recoveries which neglect the subsonic-diffuser losses. The 2° attitude was chosen for the summary plots because it approximates the design attitude of the aircraft. The effects of varying the porosity and extent of the porous surface on the ramp of inlet A were investigated at Mach numbers of 1.61 and 1.82, and these data are presented in figure 13. Figure 14 summarizes the effect on pressure-recovery and drag characteristics of varying the extent of the porous-ramp surface at $M = 1.82$.

The pressure-recovery and drag data obtained from inlet B with solid-splitter surfaces and with splitter half-angles of 3°, 7°, 10°, and 14° are presented in figure 15. Corresponding data with a splitter half-angle of 10° and porous-splitter surfaces (1-BC) are presented in figure 16. A summary of the pressure-recovery data at an angle of attack of 2° from figures 15 and 16 is presented in figure 17 as a function of the splitter half-angle. An estimated pressure recovery is also included in this figure. The effects of varying the extent of the porous surface on the splitter of inlet B and of varying the boundary-layer bleed height h at $M = 1.61$ are shown in figures 18 and 19, respectively. The results of a brief investigation of the effects of yaw on the buzz characteristics of inlets A and B are presented in figure 20.

A summary of the drag and thrust-minus-drag characteristics for inlets A and B are presented in figures 21 and 22, respectively. The method of computing the thrust-minus-drag parameter is similar to that presented in reference 2. The net value of thrust minus drag is referenced to the thrust at 100-percent pressure recovery. The actual thrust was assumed to be proportional to the compressor pressure recovery, and the inlet size was varied to supply the correct amount of air to the engine. The amount by which the inlet area was varied is also presented in figures 21 and 22 as the ratio of matched inlet to model inlet areas. Details of the calculations of thrust minus drag are presented in the appendix.

Comparisons of the total-pressure distributions in the subsonic diffusers of inlets A and B, with and without porous suction, are shown in figures 23 and 24, respectively. Typical total-pressure distributions at the compressor face of both inlets are presented in figures 25 and 26.

The lift and pitching-moment characteristics of inlets A and B are presented in figures 27 and 28, respectively, as a function of angle of attack. These data were obtained by averaging the results obtained at

various mass-flow ratios. The effects of mass-flow ratio on the lift and pitching-moment characteristics were negligible. The lift, drag, and pitching-moment characteristics of the faired-nose configurations are shown in figures 29 and 30. These latter configurations were tested to provide a correlation between the inlet data of this investigation and other stability investigations which were made with the faired-nose configurations. No discussion of the lift and pitching-moment data is presented in this report.

The engine characteristic used to compute the thrust-minus-drag parameter $\frac{T - D}{T_I}$ is shown in figure 31.

DISCUSSION OF RESULTS

Pressure-Recovery and Buzz Characteristics

Inlet A at $\alpha = 2^{\circ}$.- The maximum pressure recoveries (fig. 12) of the solid-ramp configurations were about 0.95, 0.91, and 0.86 at Mach numbers of 1.41, 1.61, and 1.82, respectively. These recoveries are from 0.04 to 0.09 lower than the estimated values. These estimated values are based on a shock system consisting of one oblique and one normal shock occurring at the Mach number behind the oblique shock and do not include subsonic losses. It was assumed that the free-stream Mach number existed at the inlet, and the compression angle of the oblique shock was made 2° larger than the corresponding ramp angle to account for the angle of attack of the inlet. In general, the differences between the estimated and experimental recoveries increase as the Mach number ahead of the normal shock of the inlet increases. Use of the porous surface (1-AE) to reduce the boundary-layer thickness on the 12.5° ramp resulted in maximum pressure recoveries which were about 0.03, 0.04, and 0.05 higher at Mach numbers 1.41, 1.61, and 1.82, respectively, than the corresponding recoveries of the solid-ramp configuration. The mass-flow ratio at which the maximum pressure recovery of each configuration was obtained varied with ramp angle and Mach number. For the solid-ramp configurations, this variation was, in general, due to the vertical sweep of the inlet lips which corresponded to the sweep of an oblique shock generated by a 2.6° ramp angle at a Mach number of 1.61, or an 8.0° ramp angle at a Mach number of 1.82.

The porous-ramp data at a Mach number of 1.82 (fig. 14) indicate that use of a porous- instead of a solid-ramp surface from stations A to C increased the maximum pressure recovery from 0.86 to 0.91. Further extension of the porous surface from stations C to E increased the maximum recovery by only 0.01. The latter part of the porous ramp was probably in the subsonic diffuser at maximum pressure-recovery conditions.

The relative merits of removing the boundary layer ahead or behind the normal shock of the inlet cannot be determined from these tests, however, because no tests were made with a porous surface from stations C to E only.

The amount of air which passed through the porous surfaces was not measured during these tests. The static pressures on the exit side of the porous surfaces were measured at Mach numbers of 1.41 and 1.82 and were found to have a maximum value which was about 10 percent above free-stream static pressure. However, the validity of using a calculated pressure difference with the data of figure 8 to determine the flow through the surface is questionable (ref. 1) because of the high flow velocity parallel to the ramp surface. Consequently, it is not possible to deduce quantitatively from the data obtained with different degrees of porosity (fig. 13) the effect of the rate of air removal on maximum pressure recovery.

It is apparent from the preceding discussion that the boundary layer of the ramp had an adverse effect on the pressure recovery of inlet A. The data are not sufficiently complete to evaluate the magnitude of the boundary-layer losses, but these losses are shown to be at least 3 to 5 percent of the free-stream stagnation pressure, the losses increasing as the Mach number ahead of the normal shock is increased.

At supercritical conditions (fig. 13) the mass-flow ratios of porous configurations 1-AB, 2-AC, and 3-AE were greater than those of the solid-ramp configurations. For configurations 1-AB and 2-AC this increase probably resulted from a reduction of the effective ramp angle due to the boundary-layer removal through the porous surfaces so that more air was permitted to enter the inlet at supercritical conditions. This additional increment of air was larger than the amount removed by the porous surface. For configuration 3-AE, rough calculations have indicated that, at supercritical conditions where the pressure recovery is low, the static pressures ahead of the diffuser normal shock may have been low enough to draw a part of the additional increment of air through the porous air exit into the inlet duct.

It may be noted for most of the porous ramp configurations that, at supercritical conditions, the mass flow continues to increase as the pressure recovery decreases. When the normal shock moves farther down in the diffuser, a smaller pressure difference exists across a larger part of the porous surface and, as a result, the air flow through the porous surface decreases. As mentioned in the previous paragraph, the air flow may actually reverse under certain conditions. Inasmuch as the amount of air entering the inlet remains constant under these conditions, the mass flow passing the compressor face must increase.

The buzz characteristics of inlet A with solid ramps (fig. 10) were primarily a function of Mach number. At a Mach number of 1.41 the range of stable mass-flow ratio varied from about 0.45 to 0.55. As the Mach number increased, the stable range decreased, and at a Mach number of 1.82 the range was about 0.02 and 0.06 for the 8° and 12.5° ramp angles. Neglecting the increasing mass-flow ratios at supercritical conditions, the use of the porous surface (figs. 11 and 13) resulted in only small changes in the stability range of the inlet.

Inlet B at $\alpha = 2^{\circ}$.- The maximum measured pressure recoveries (fig. 17) at Mach numbers of 1.41, 1.61, and 1.82 with the solid splitters were about 0.94, 0.91, and 0.85, respectively. All these recoveries were obtained with the 7° half-angle splitter. At higher splitter half-angles the measured pressure recoveries decreased although, in general, the estimated recoveries continued to increase. These estimated recoveries were based on a shock system consisting of two oblique shocks and one normal shock which occurred at the Mach number behind the second oblique shock. The compression angle of the first oblique shock was 3.0° and that of the second oblique shock varied with splitter half-angle. The free-stream Mach number was assumed to exist at the inlet, and the effects of subsonic diffusion were neglected. The rise of static pressure across the oblique shocks formed by the 7° half-angle splitter was approximately the same for the three test Mach numbers. Inasmuch as these shocks lay ahead of the lip of the boundary-layer bleed, it may be that the higher pressure rise associated with the larger splitter angles had some adverse effect on the radome-nose boundary layer which reduced the effectiveness of the bleed system. The maximum pressure recoveries of the porous splitter (1-BC) were about 0.05 to 0.06 higher than the recoveries of the corresponding solid-surface splitter (fig. 17). The data of figure 18 indicate that removal of more of the corner boundary layer, by use of the small gap (fig. 5, section BB) at the corners formed by the top of the splitter and the inlet, apparently improved the maximum pressure recovery by 0.02. Inasmuch as surface CD is in the subsonic diffuser, the elimination of the porous splitter in this region probably had no adverse effect on the pressure recovery.

Elimination of the boundary-layer bleed reduced the maximum pressure recovery by about 0.01 (fig. 19). Apparently the fuselage fairing (fig. 5) which was used to eliminate the bleed system was about as effective as the bleed system in diverting the boundary layer of the fuselage from the inlet. The effectiveness of the faired fuselage may have been due to its effect on the local static-pressure distribution rather than to an actual diverting action. The original fuselage shape ahead of the inlet probably created low local static pressures and thus caused a thickening of the boundary layer ahead of the inlet. Use of the fuselage fairing may have prevented the local thickening of the boundary layer by making the static-pressure distribution more positive.

The stable mass-flow range for all the solid-splitter configurations (fig. 15) was about the same at a given Mach number but decreased from an average value of about 0.23 at a Mach number of 1.41 to a value of 0.06 at a Mach number of 1.82. In general, the use of porous surfaces did not significantly affect the inlet stability range (figs. 15, 16, and 18).

Effects of angle of attack on inlets A and B.- The effect of angle of attack on the pressure recovery of inlet A (fig. 10) varies with Mach number and ramp angle. In general, increasing the angle of attack either increased the pressure recovery or had no effect. The largest increases were obtained with the configurations having compression angles at 2° angle of attack which were appreciably less than the compression angle required for optimum recovery. In general, the change in buzz characteristics was small. For the 8° ramp, however, large increases in the range of stable mass flow occurred at Mach numbers of 1.41 and 1.61 when the angle of attack increased from 4° to 6°.

The effects of angle of attack on pressure recovery and buzz of inlet B were small. These small effects might be expected because the compression angles were essentially independent of the angle of attack for the range of these tests.

Yaw effects.- The data of figure 20 indicate that the yaw effects on the pressure recovery of the inlet and minimum stable mass-flow ratio were insignificant for inlet A for yaw angles up to 4°. Yaw effects were relatively large for inlet B probably because of its vertical splitter. On the latter inlet, the pressure recovery decreased and stable mass-flow range decreased as the yaw angle increased at Mach numbers of 1.41 and 1.61. The pressure-recovery data obtained at positive and negative angles of yaw were slightly different because of the compressor-rake design. These differences are illustrated in the data at a Mach number of 1.82.

Drag and Performance

Inlet A.- The external drag was about the same (fig. 21), at a given mass-flow ratio for the three solid-ramp configurations at 2° angle of attack. At mass-flow ratios where an appreciable amount of air was spilled subcritically, the drag of the porous ramp was lower than that of the corresponding solid-ramp configuration. Inasmuch as all the drag produced by removing the air through the porous surface was included in the external drag coefficient, these data indicate that spillage through the porous surface created less drag than spillage by means of a normal shock. As the supercritical mass-flow ratio was approached, the drag difference between the two configurations decreased and, at Mach numbers of 1.41 and 1.61, the supercritical drag of the porous ramp was higher than that of the solid ramp.

The high external drag of the 12.5° ramp resulted in low maximum-thrust parameters at Mach numbers of 1.41 and 1.61. Use of the porous- instead of the solid-ramp surface increased the maximum-thrust parameter by increments of about 0.02 to 0.05, the larger increments occurring at the higher Mach numbers.

Inlet B.- The data of figure 22 indicate that at Mach numbers of 1.41 and 1.61 the external drag coefficients for a given mass-flow ratio vary appreciably with splitter half-angle.

The maximum-thrust parameters of the solid splitters were obtained with the 3° and 7° splitters. At the larger splitter half-angles the decrease of pressure recovery and increase of external drag resulted in large decreases in the thrust parameter. Use of the porous splitter resulted in maximum-thrust parameters which were about 0.01, 0.05, and 0.06 higher than those of the corresponding solid-splitter values at Mach numbers of 1.41, 1.61, and 1.82, respectively. Elimination of the boundary-layer bleed had no effect on the maximum-thrust parameter of the inlet with the solid 10° splitter.

Diffuser Total-Pressure Distribution

The total-pressure surveys which were made in the subsonic ducts of both inlets (figs. 23 and 24) indicate that the use of the porous ramp and splitter surfaces resulted in significant increases in the local total pressures in parts of the diffusers. It is interesting to note on inlet B (fig. 24) that the total pressures were relatively independent of the distance from the splitter but were dependent upon the distance from the top surface of the duct. Apparently, the curvature of the duct (fig. 5) and the resultant static-pressure distribution across the duct forced a large part of the splitter boundary layer to the top duct surface. Therefore, as the porous surface reduced the splitter boundary-layer thickness, the local total pressure near the top of duct increased appreciably.

The typical total-pressure distributions at the compressor face (figs. 25 and 26) indicate that for both inlets the total-pressure variation decreases as the compression angle increases. The use of the porous surfaces increased the overall level of the total pressure but did not decrease the variation of the total pressure across the compressor face.

CONCLUSIONS

An investigation of the pressure-recovery and force characteristics of 1/10-scale models of two inlet configurations of fighter-type aircraft has been made at Mach numbers of 1.41, 1.61, and 1.82. One model, inlet A,

had a nose inlet incorporating a horizontal-ramp compression surface. The second model, inlet B, had a chin-scoop inlet incorporating a vertical-wedge splitter. Based on this investigation, the following conclusions were made:

1. The maximum pressure recoveries obtained at Mach numbers of 1.41, 1.61, and 1.82 from inlets A and B at an angle of attack of 2° were about 0.95, 0.91, 0.86, and 0.94, 0.91, and 0.85, respectively. These recoveries were from 0.04 to 0.09 lower than estimated recoveries which neglected subsonic losses.

2. The range of stable mass flow of both inlets was primarily a function of Mach number. For inlet A, the stable range decreased from an average value of about 0.50 to 0.04 as the Mach number increased from 1.41 to 1.82. The corresponding values for inlet B were about 0.23 and 0.06.

3. The effects of angles of attack and yaw on inlet pressure recovery were consistent with the geometry of the two inlets. Increasing the angle of attack had some beneficial effect on the pressure recovery of inlet A but little effect on inlet B. Increasing the angle of yaw had a detrimental effect on the pressure recovery and buzz characteristics of inlet B but little effect on inlet A.

4. The use of area suction on the inlet compression surfaces resulted in maximum pressure recoveries which were 0.02 to 0.06 higher than the recoveries of similar configurations without area suction but did not significantly affect the inlet stability range.

5. The use of area suction did not result in significant changes of external drag at a given mass-flow ratio and, therefore, improved the thrust-minus-drag characteristics of both inlets.

6. Elimination of the boundary-layer bleed system of inlet B by means of a fuselage fairing had no effect on the thrust-minus-drag characteristics of the inlet.

7. The total-pressure variations at the compressor face decreased for both inlets as the compression angle increased. The use of area

suction increased the overall level of the total pressure but did not alter the variation of the total pressure across the compressor face.

Langley Aeronautical Laboratory,
National Advisory Committee for Aeronautics,
Langley Field, Va., October 21, 1954.

APPENDIX

CALCULATION OF THRUST PARAMETER

The calculation of the thrust parameter $\frac{T - D}{T_I}$ presented in figures 21 and 22 is based on the method described in reference 2. The thrust quantities are based on the characteristics of a current turbojet engine having the air flow characteristics at 35,000 feet which are presented in figure 31. The ideal thrust at 100-percent pressure recovery is indicated by the symbol T_I. The actual engine thrust T was assumed to decrease 1.25 percent for every percent loss of total pressure recovery. The inlet size was assumed to vary as required to supply the correct amount of air to the engine. The inlet drag D was varied with inlet size by assuming that the drag increment between the inlet and faired-nose configurations was proportional to inlet capture area. The maximum increment which was applied to the basic inlet drag during these computations was about 2 percent of the ideal thrust. The ratio of inlet area required for matching to model inlet area is shown in figures 21 and 22.

REFERENCES

1. Stokes, George M., Davis, Don D., and Sellers, Thomas B.: An Experimental Study of Porosity Characteristics of Perforated Materials in Normal and Parallel Flow. NACA TN 3085, 1954. (Supersedes NACA RM L53H07, 1953.)

2. Schueller, Carl F., and Esenwein, Fred T.: Analytical and Experimental Investigation of Inlet-Engine Matching for Turbojet-Powered Aircraft at Mach Numbers Up to 2.0. NACA RM E51K20, 1952.

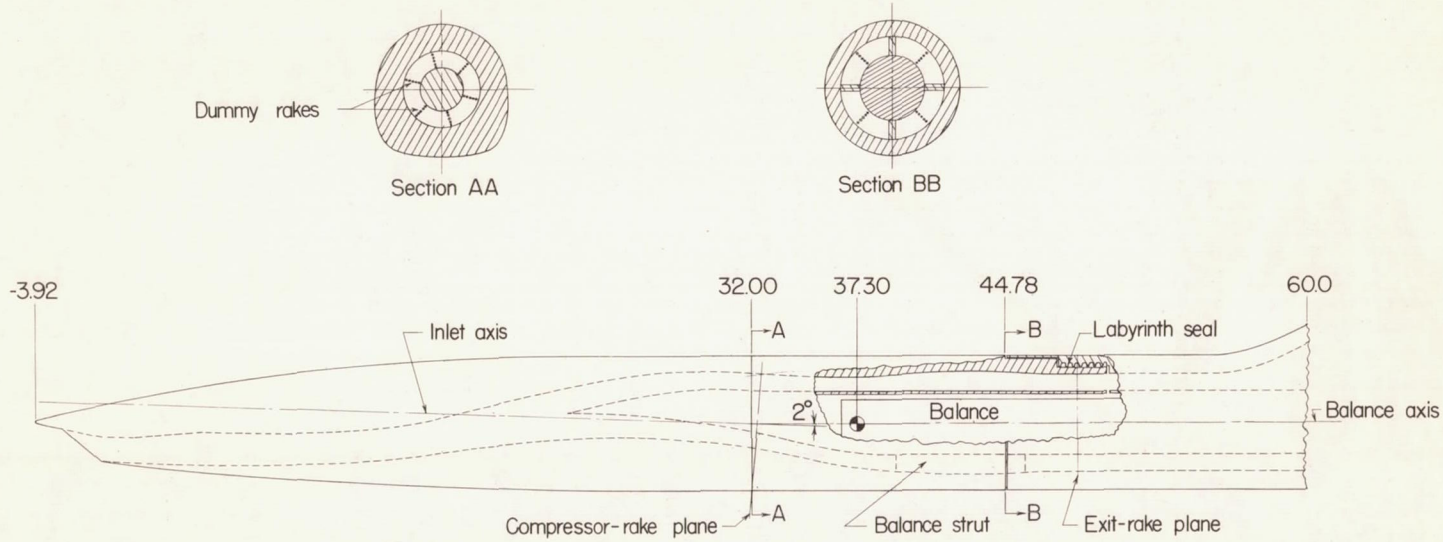

(a) Inlet forebody (balance supported).

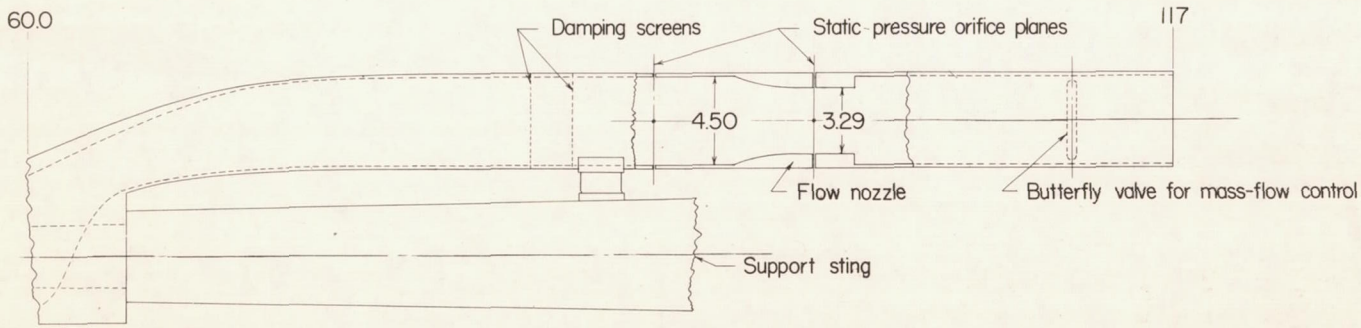

(b) Mass-flow measuring assembly (sting supported).

Figure 1.- Schematic drawing of inlet forebody and mass-flow measuring assembly. All dimensions are in inches.

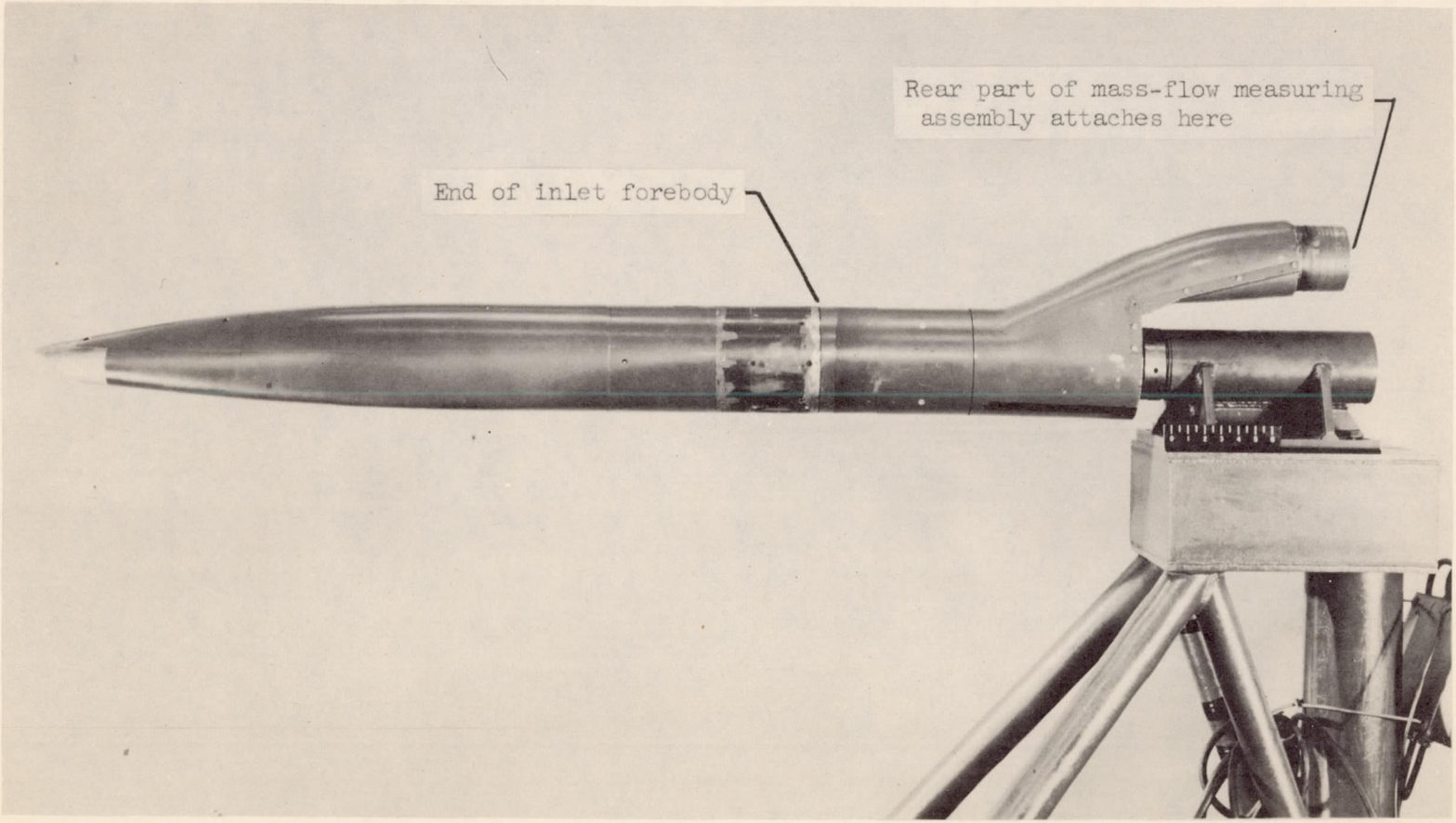

L-82927.1

Figure 2.- Model without rear part of the mass-flow measuring assembly.

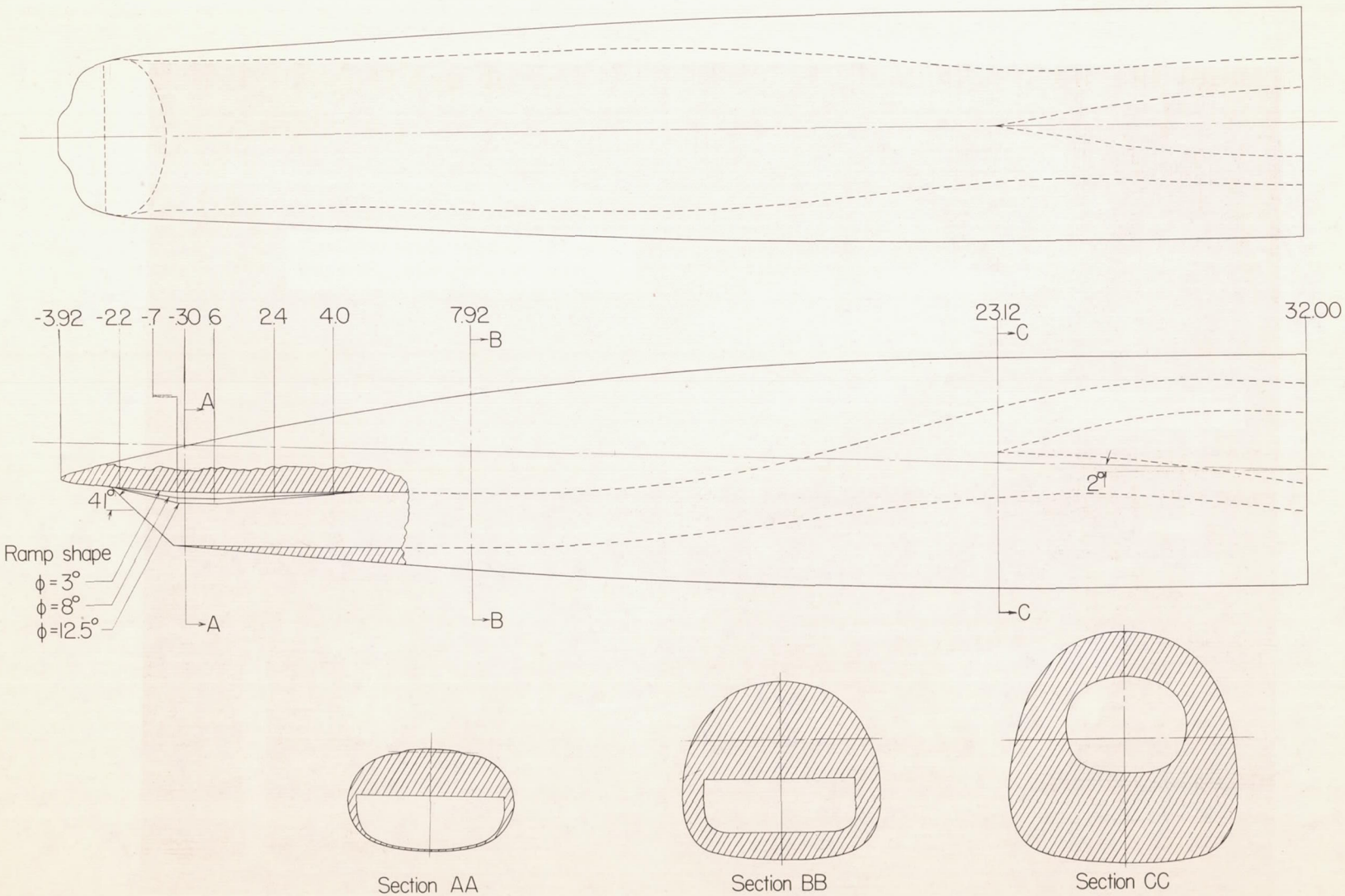

Figure 3.- Schematic drawing of inlet A. All dimensions are in inches.

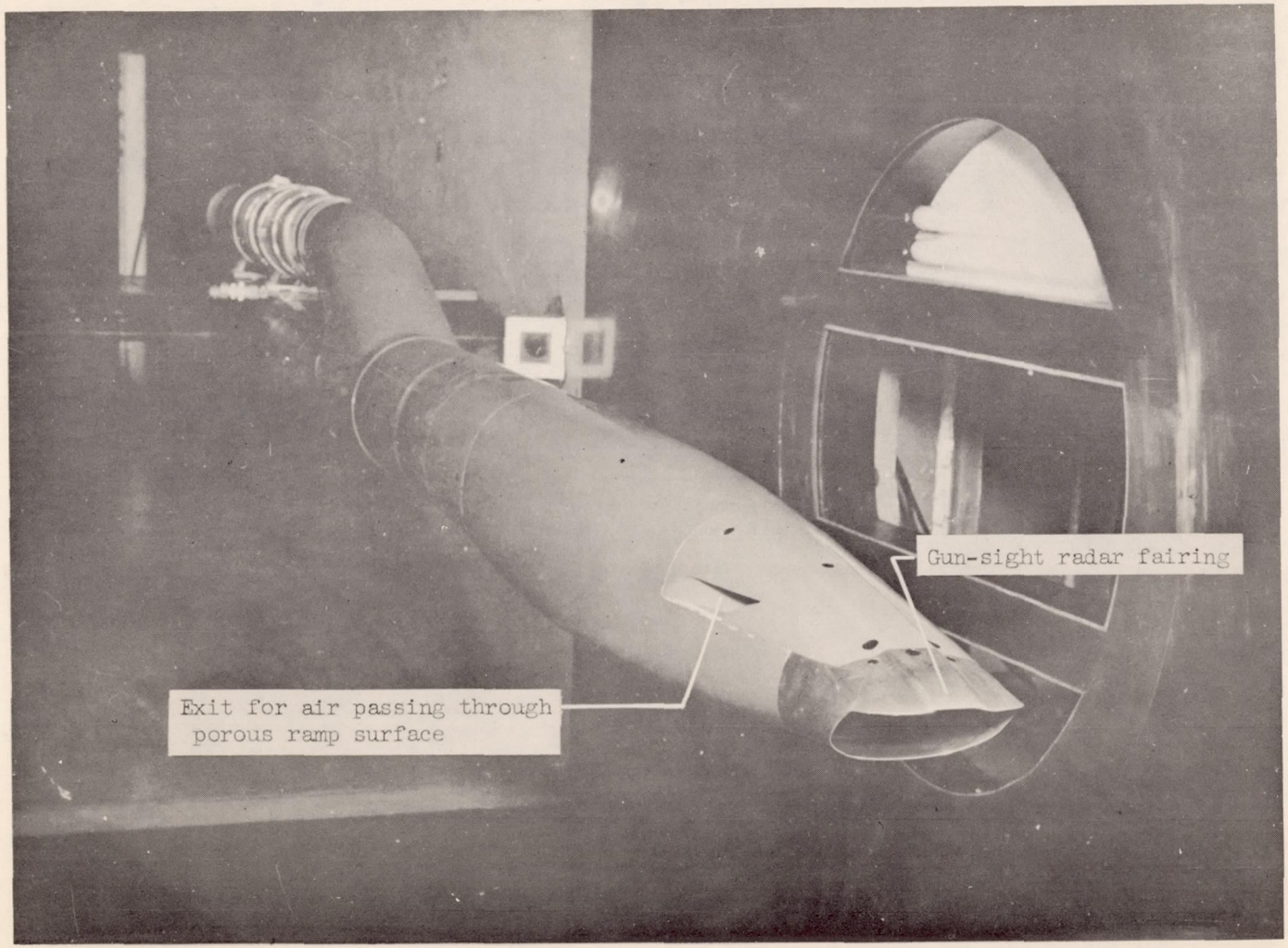

L-86445

Figure 4.- Inlet A.

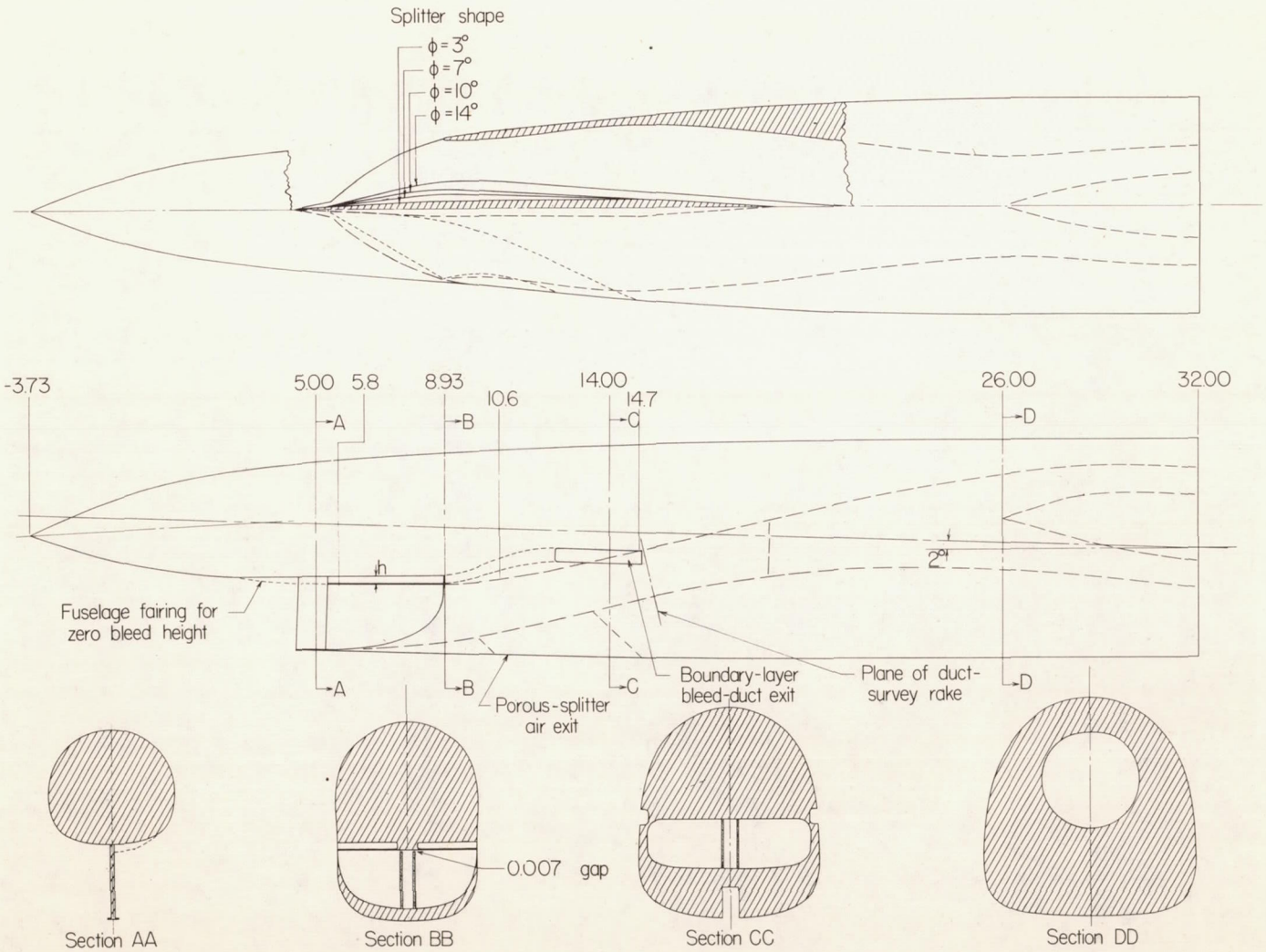

Figure 5.- Schematic drawing of inlet B. All dimensions are in inches.

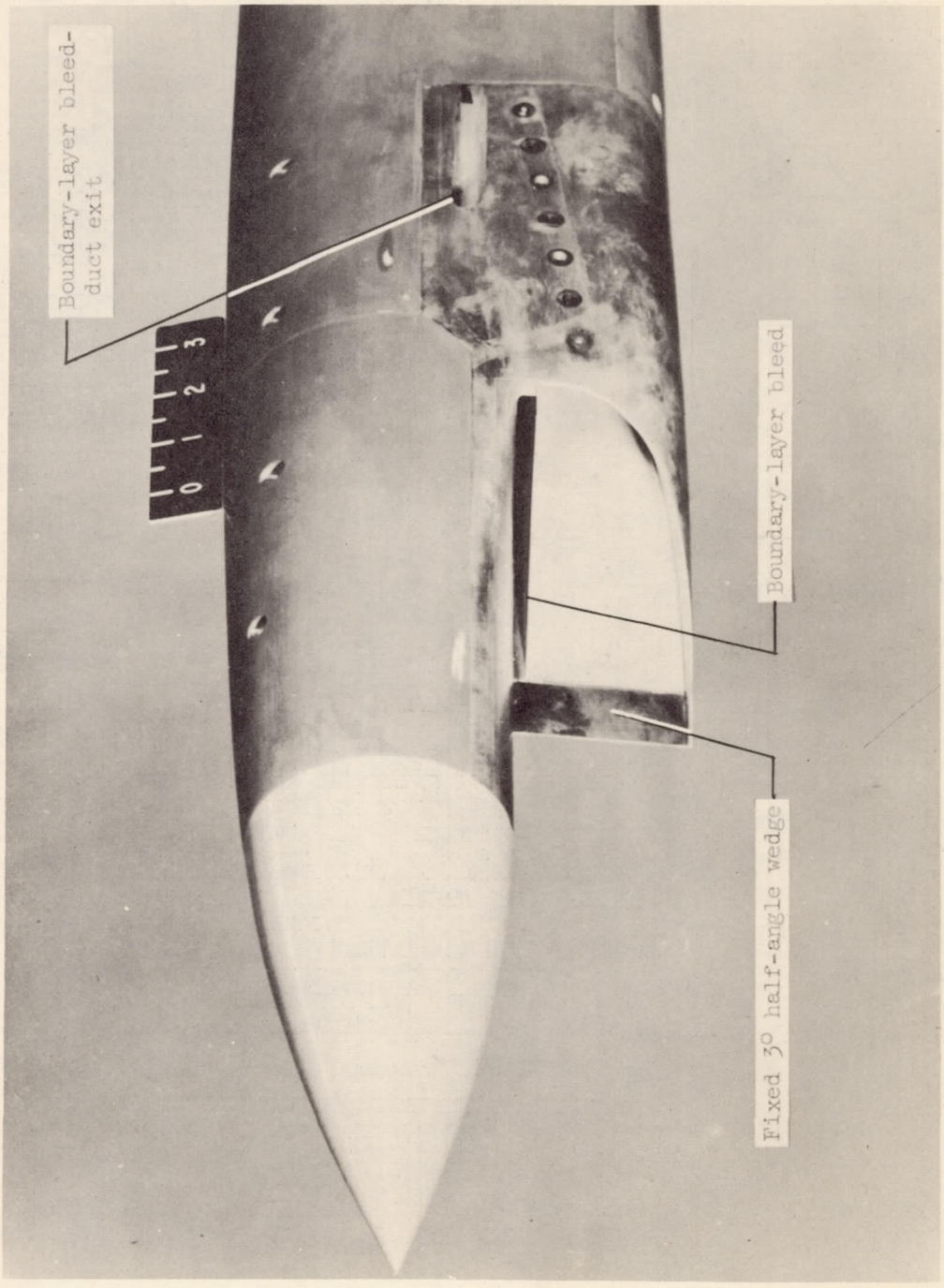

L-86446

Figure 6.- Inlet B.

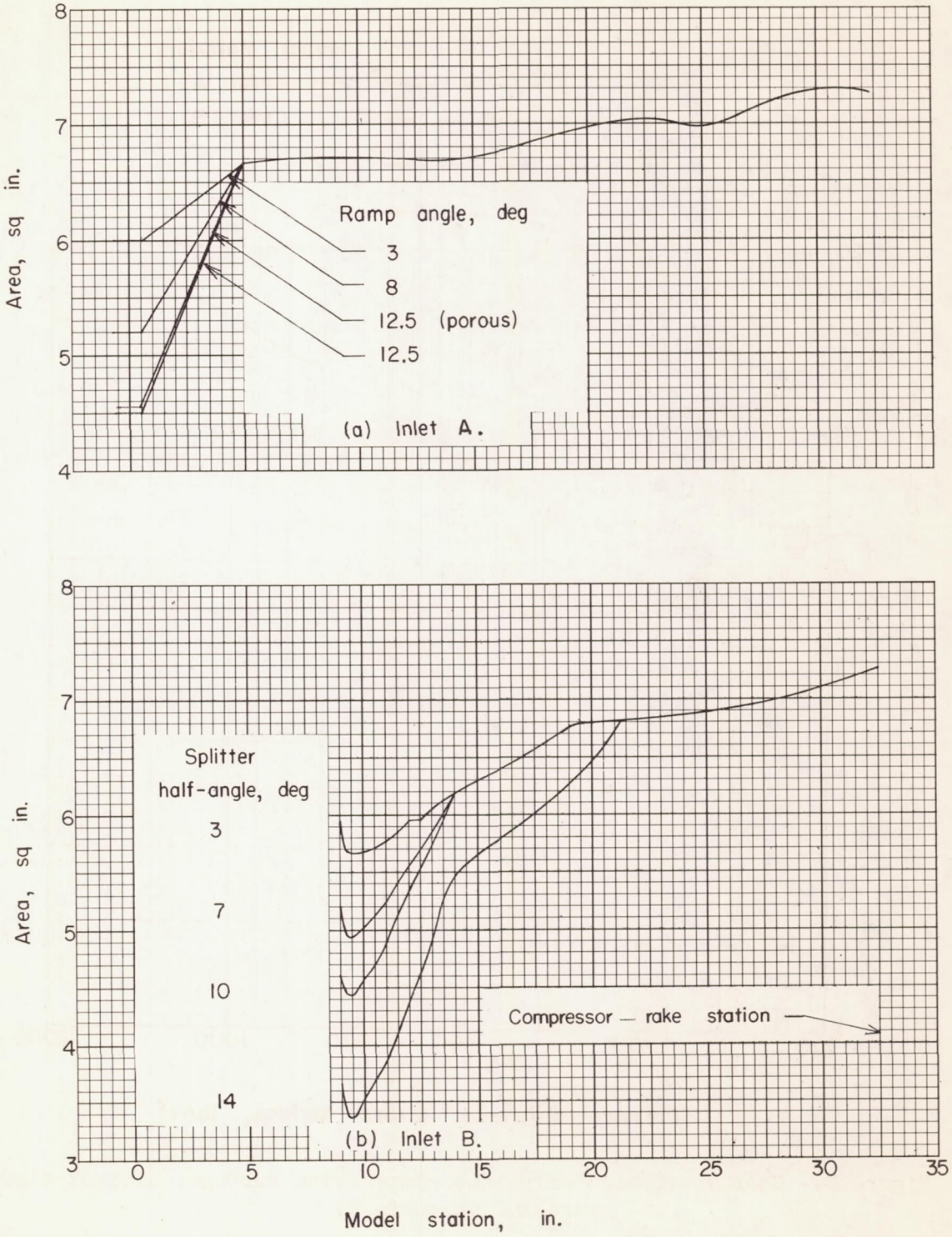

Figure 7.- Area distribution in ducts of inlets A and B.

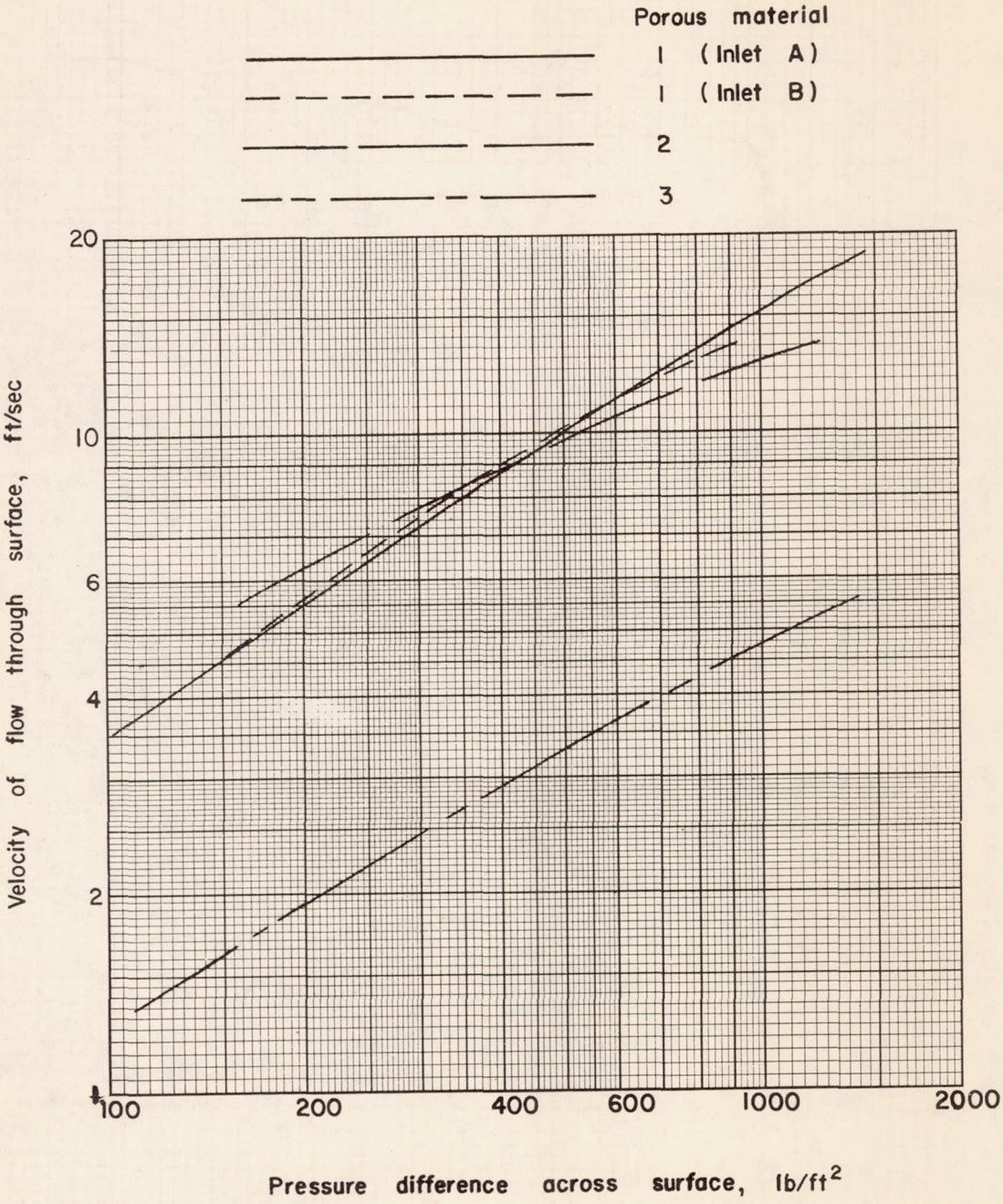

Figure 8.- Characteristics of porous compression surfaces without flow parallel to surface.

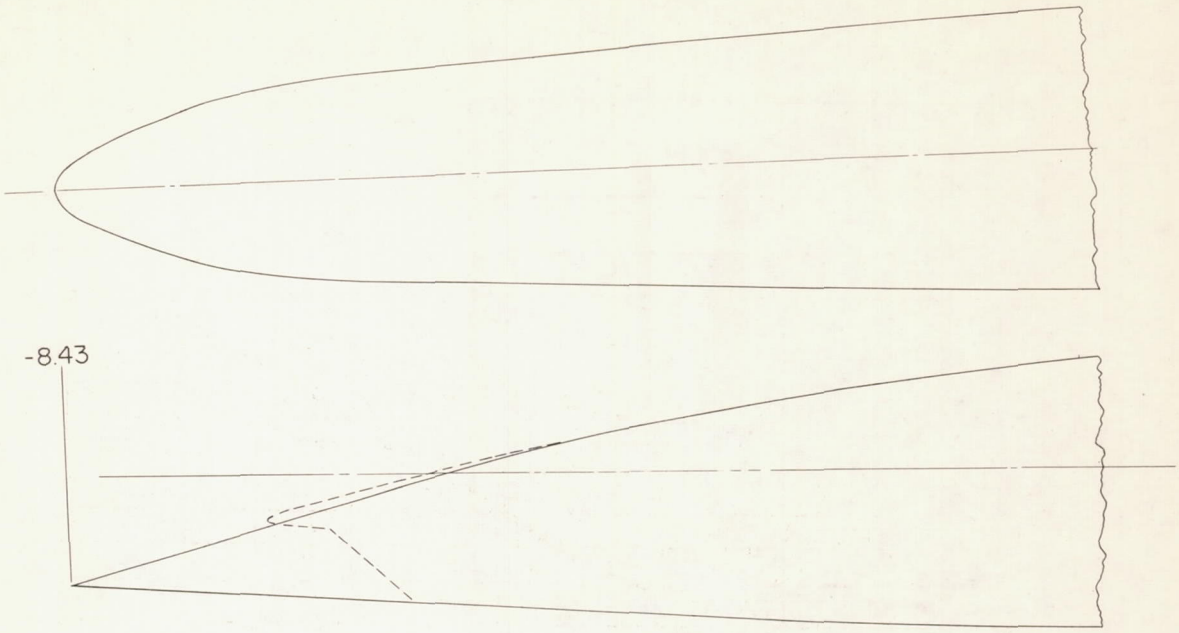

(a) Faired nose A.

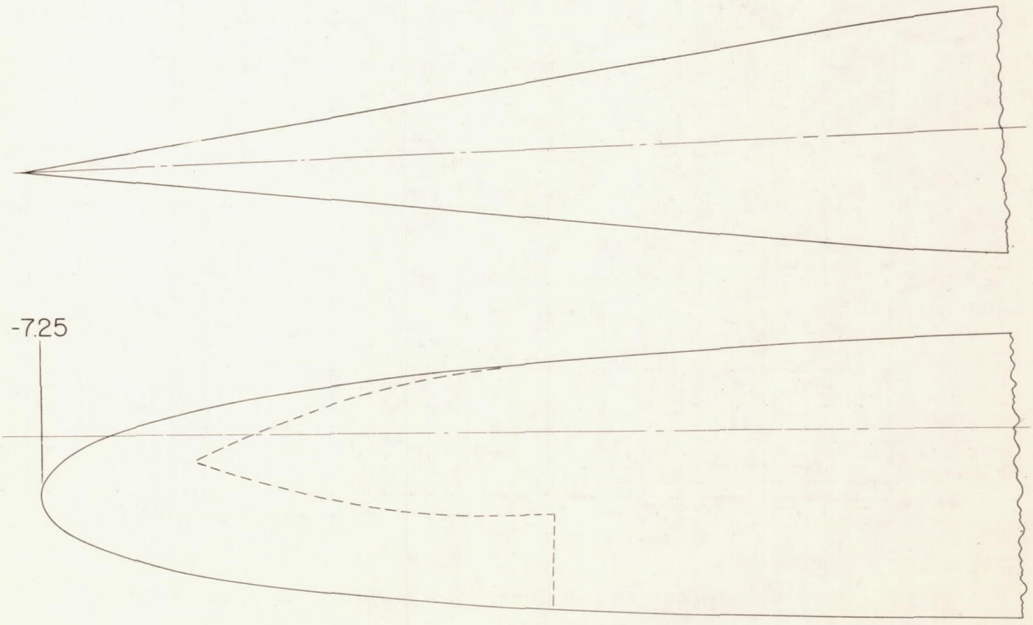

(b) Faired nose B.

Figure 9.- Schematic drawing of faired-nose configurations.

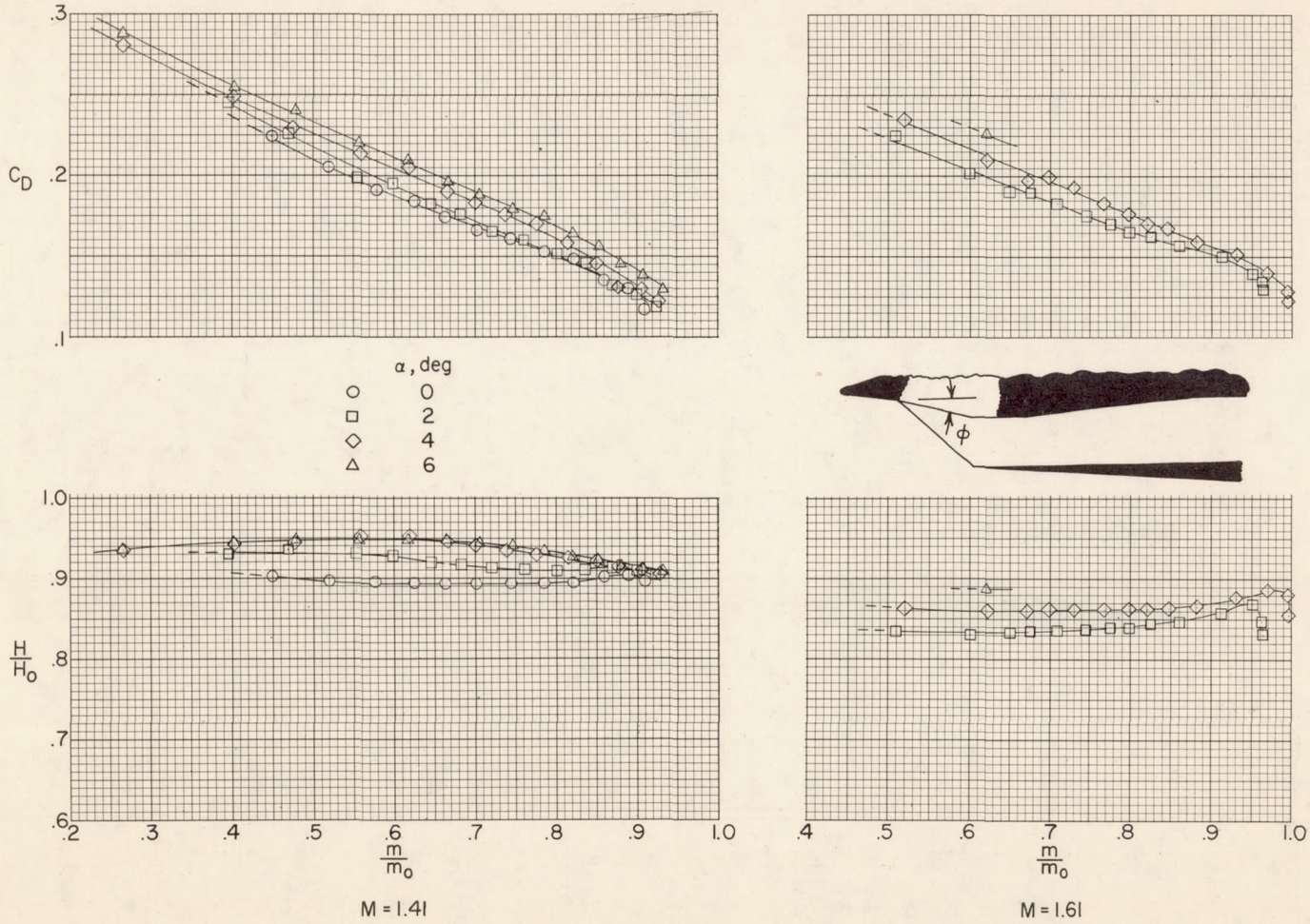

(a) $\phi = 3^{\circ}$.

Figure 10.- Pressure-recovery and drag characteristics of inlet A without porous-ramp surfaces.

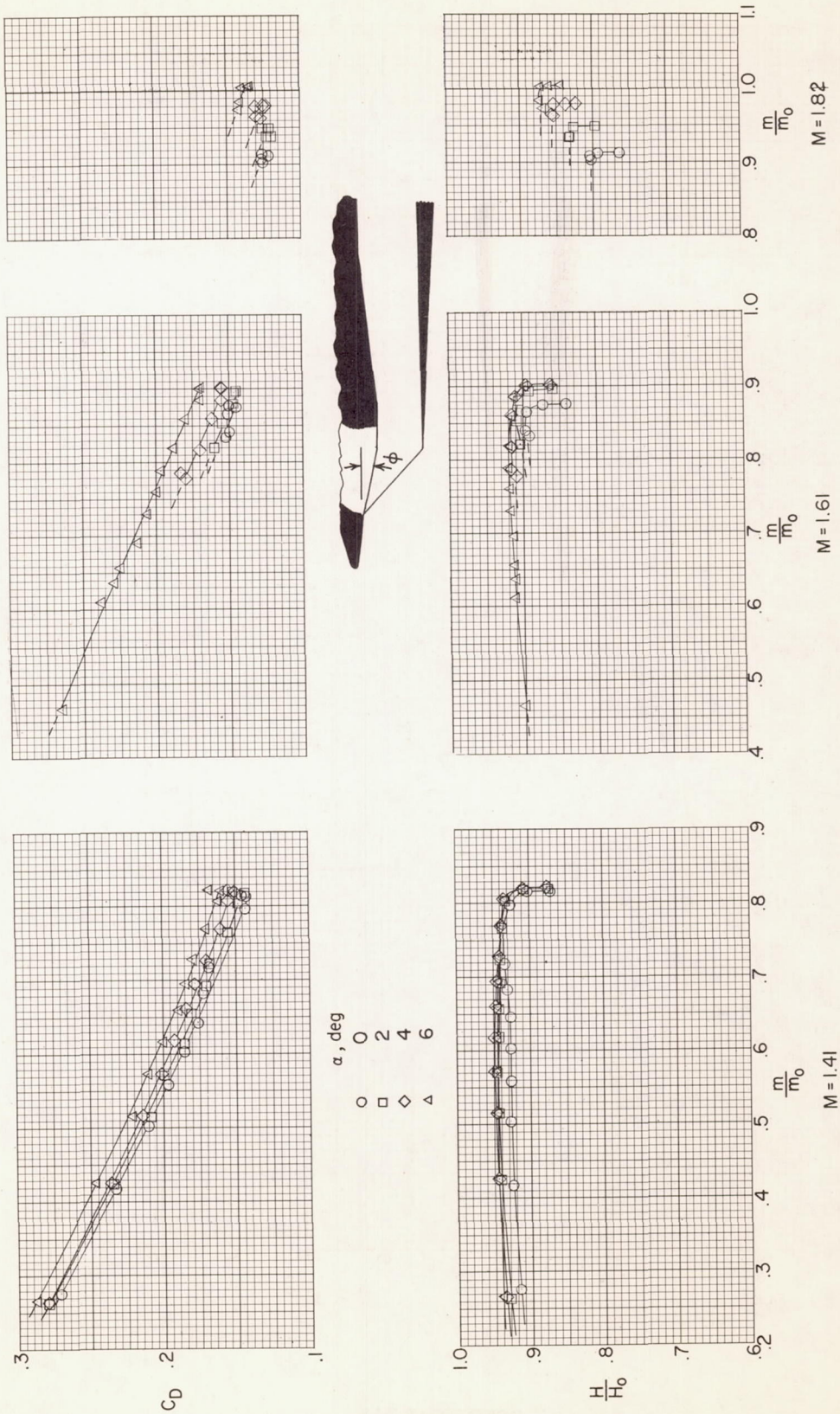

(b) $\phi = 8^{\circ}$.

Figure 10.- Continued.

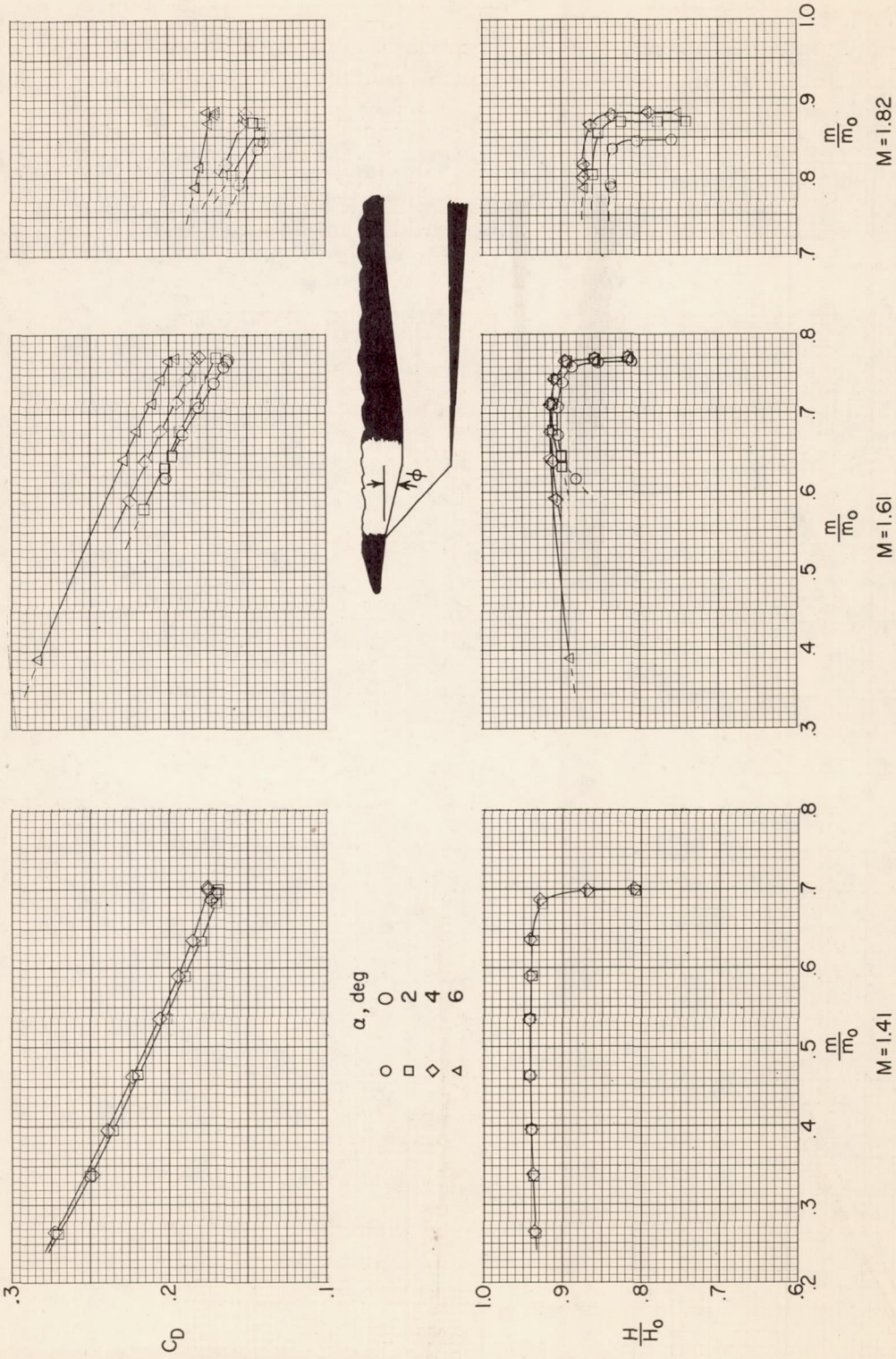

(c) $\phi = 12.5^{\circ}$.

Figure 10.- Concluded.

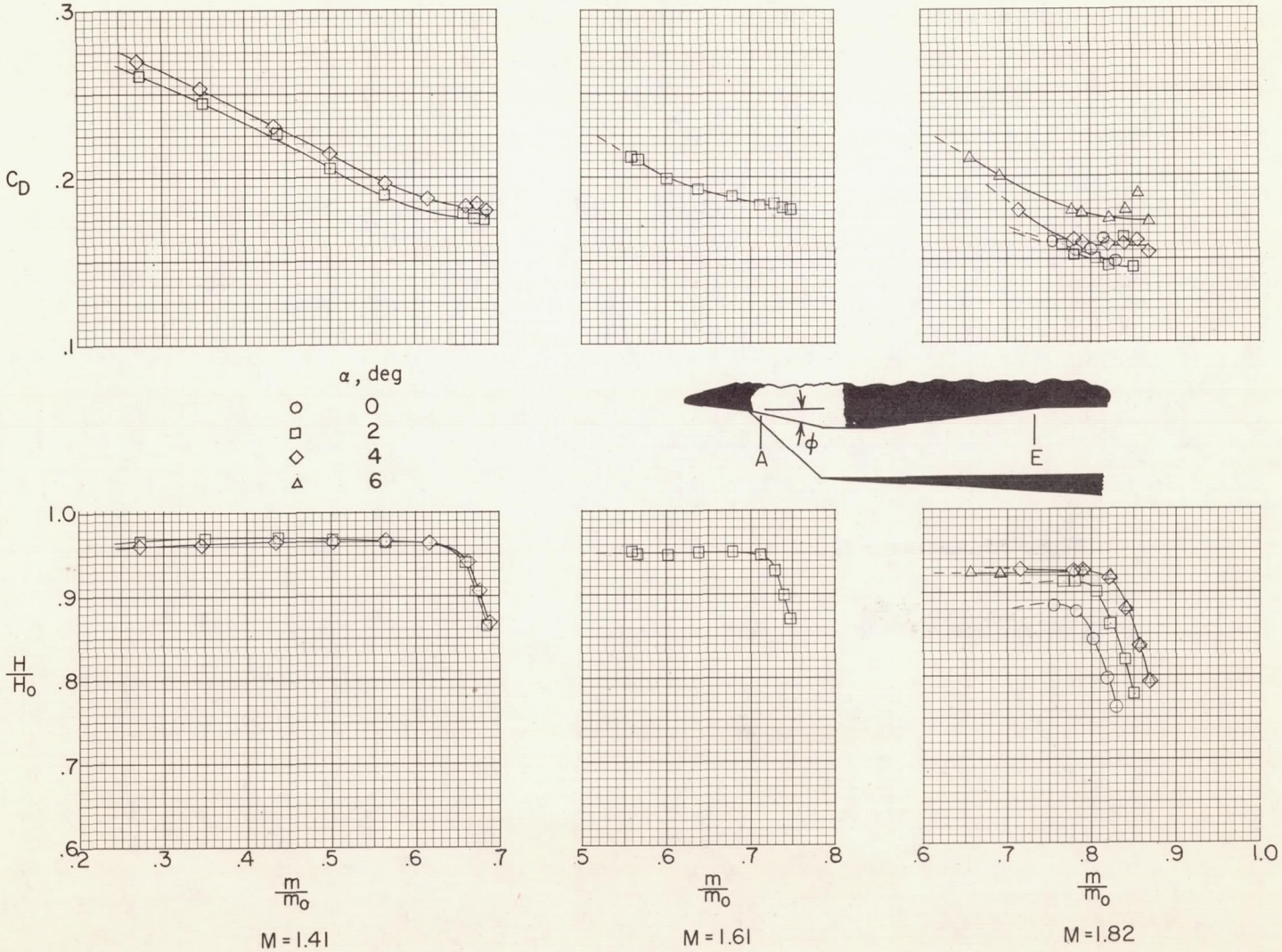

Figure 11.- Pressure-recovery and drag characteristics of inlet A with porous-ramp surface (1-AE). $\phi = 12.5^{\circ}$.

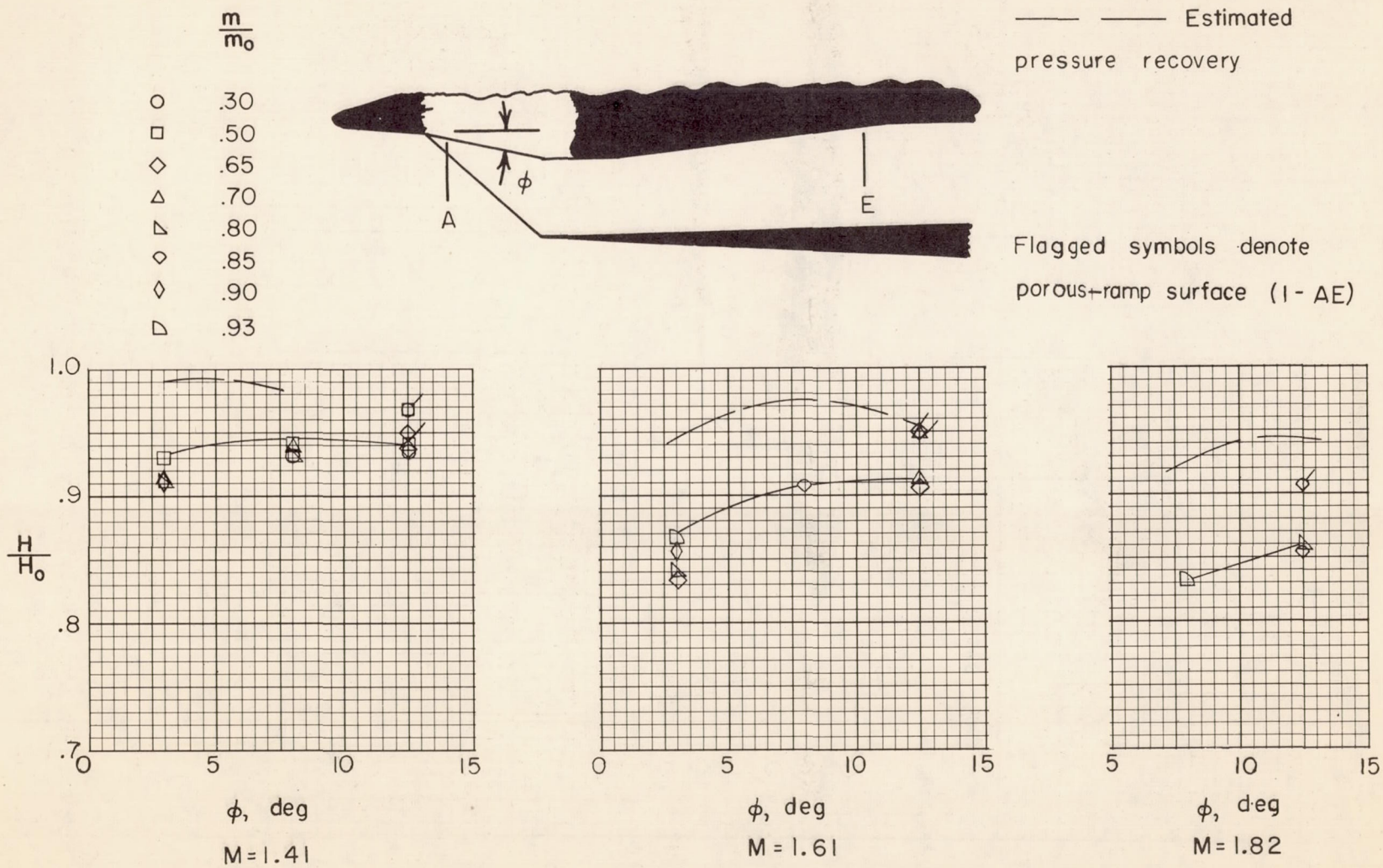

Figure 12.- Variation of pressure recovery of inlet A with ramp angle. $\alpha = 2^{\circ}$.

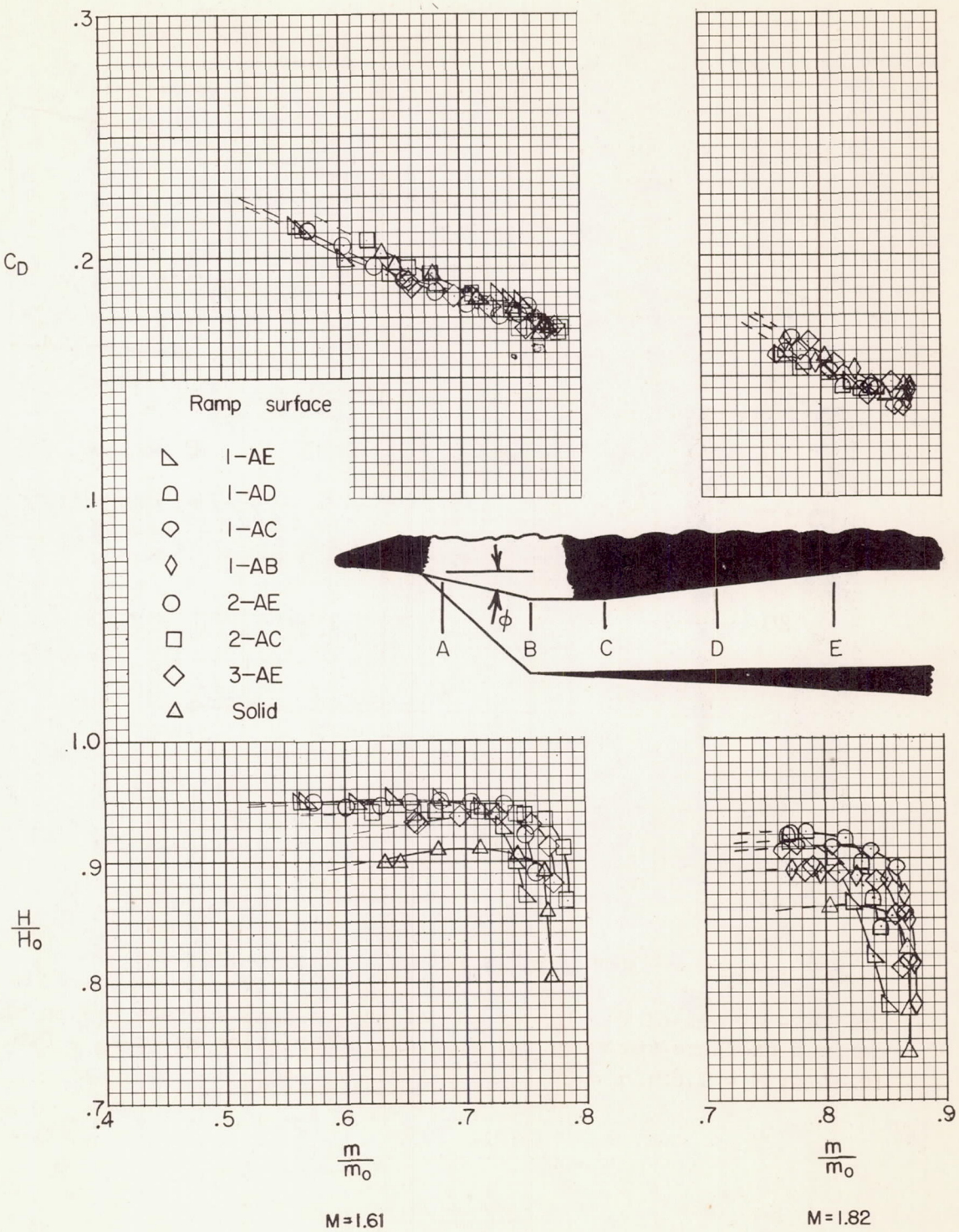

Figure 13.- Comparison of effect of several porous-ramp surfaces on pressure-recovery and drag characteristics of inlet A. $\alpha = 2^{\circ}$; $\phi = 12.5^{\circ}$.

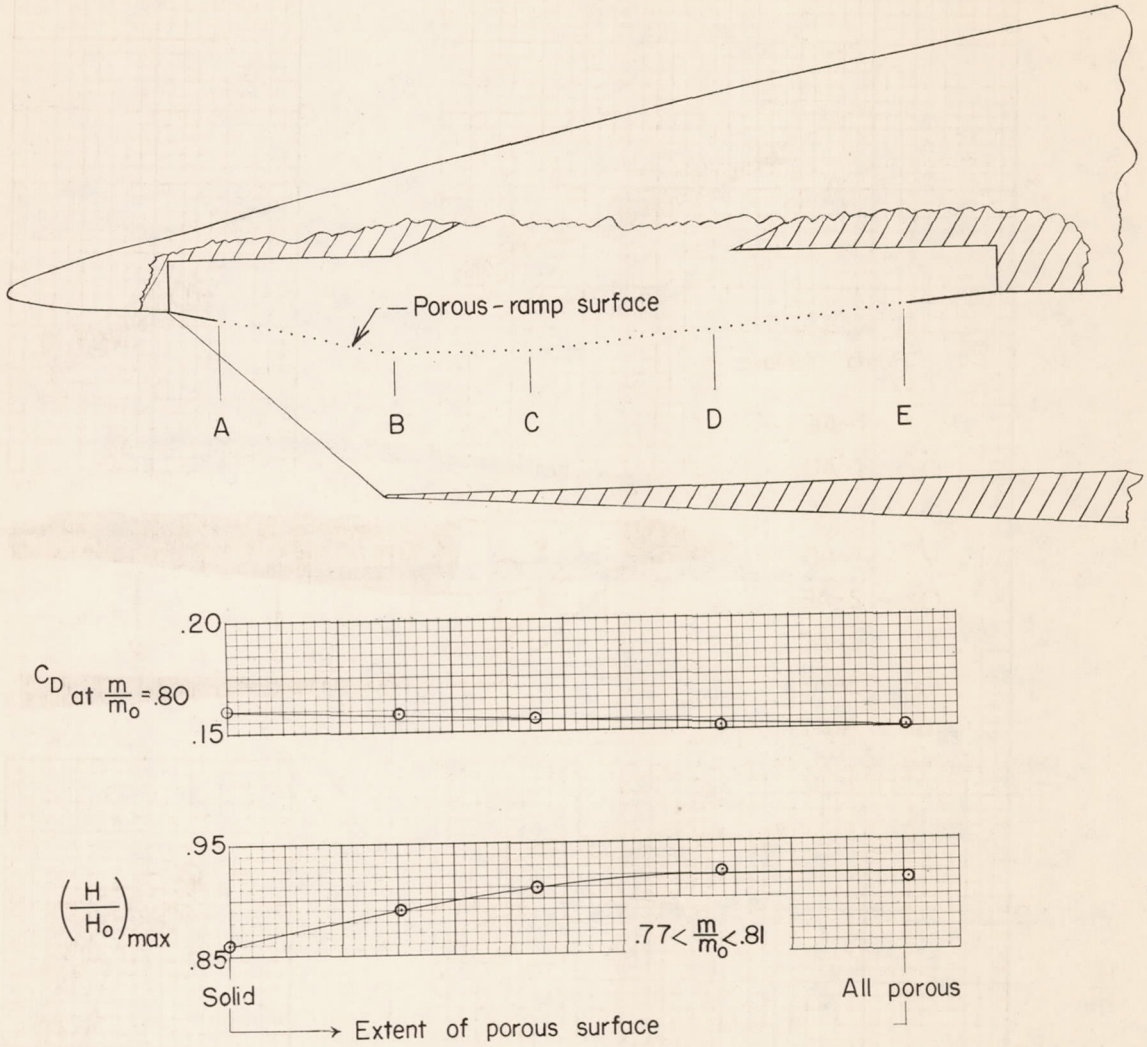

Figure 14.- Effect of varying extent of porous-ramp surface (1) on the maximum pressure-recovery and drag characteristics at $m/m_o = 0.8$. Inlet A; $M = 1.82$; $\alpha = 2^o$.

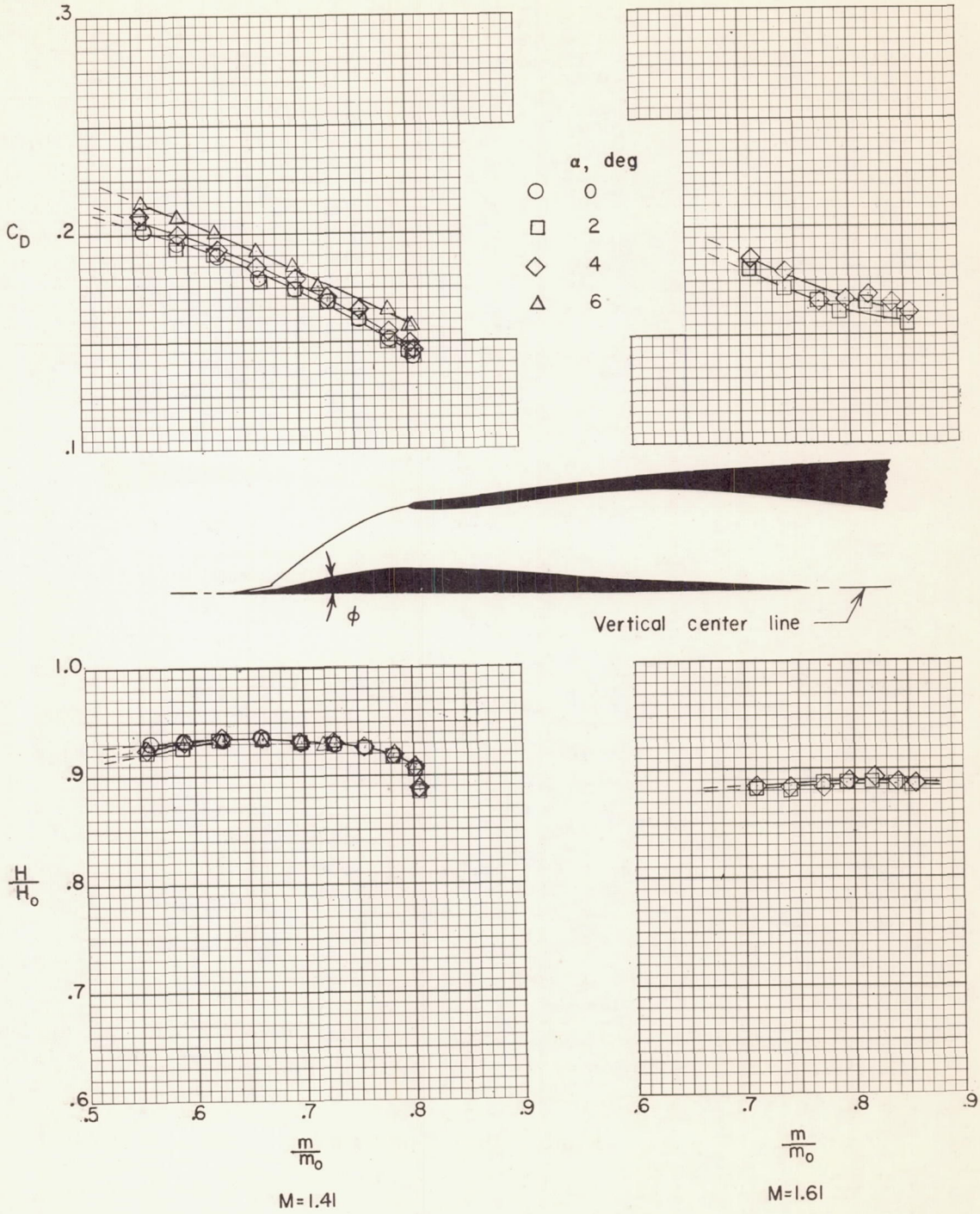

(a) $\phi = 3^{\circ}$.

Figure 15.- Pressure-recovery and drag characteristics of inlet B without porous-splitter surfaces. h = 0.21 inch.

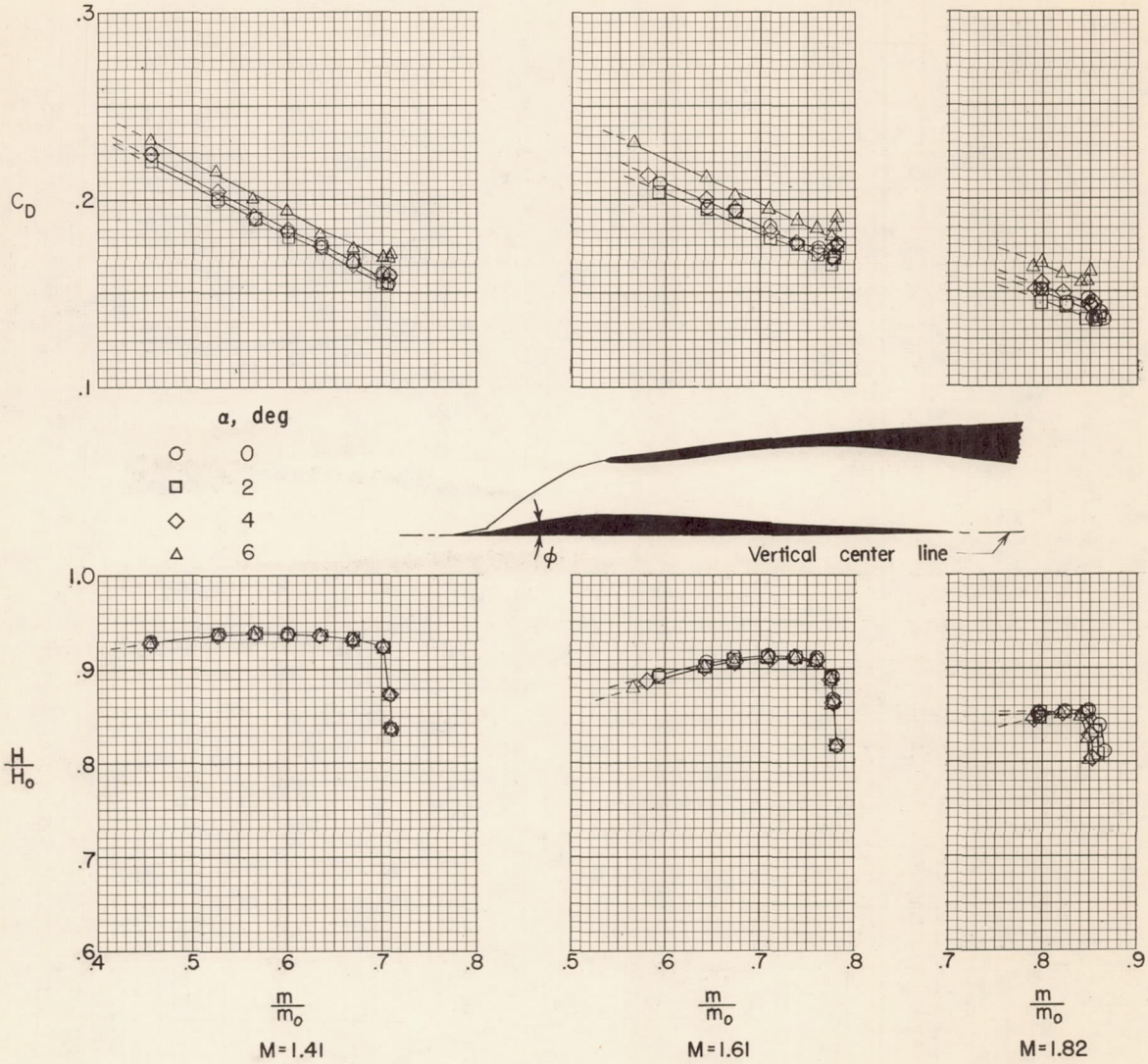

(b) $\phi = 7^{\circ}$.

Figure 15.- Continued.

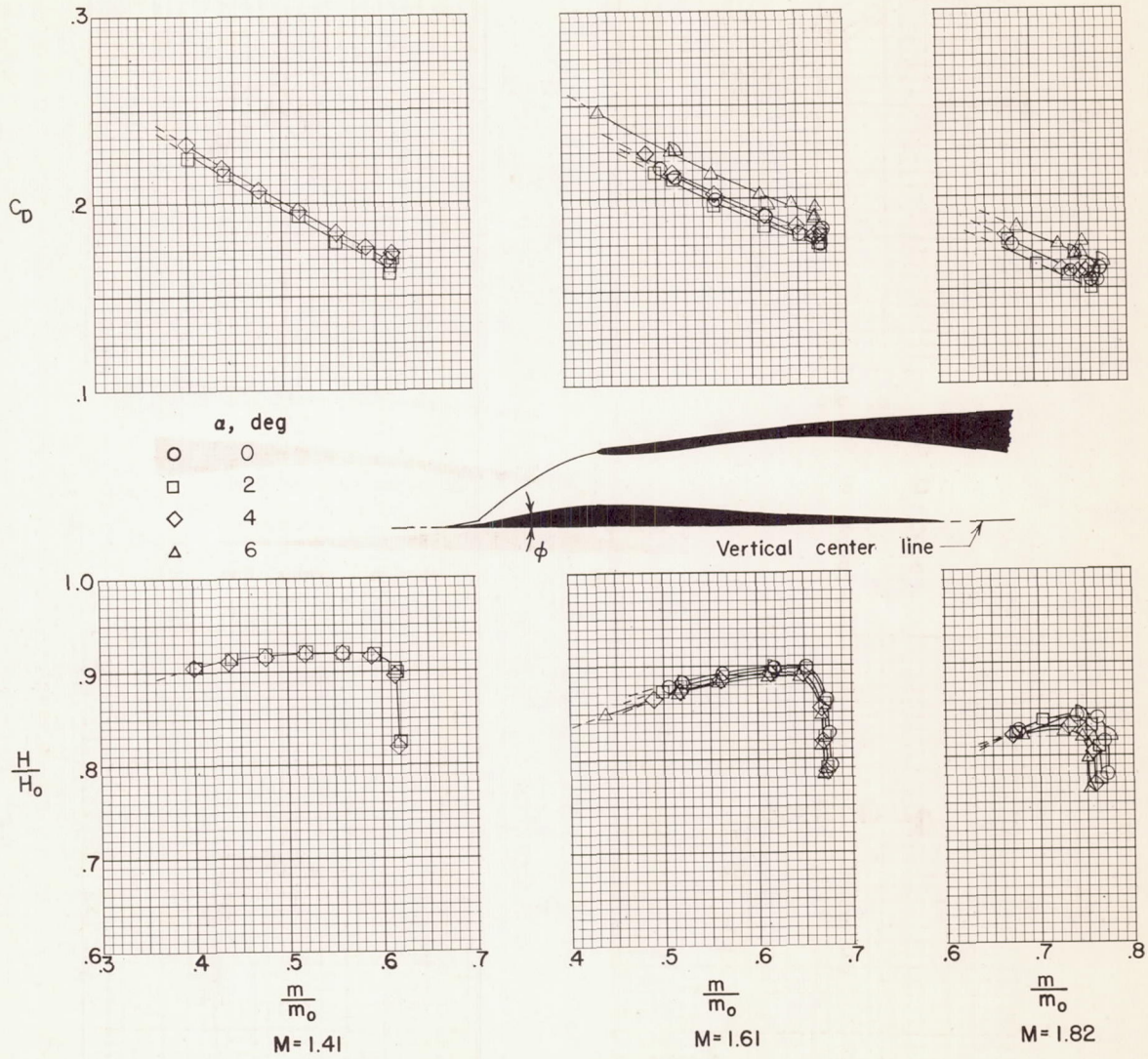

(c) $\phi = 10^{\circ}$.

Figure 15.- Continued.

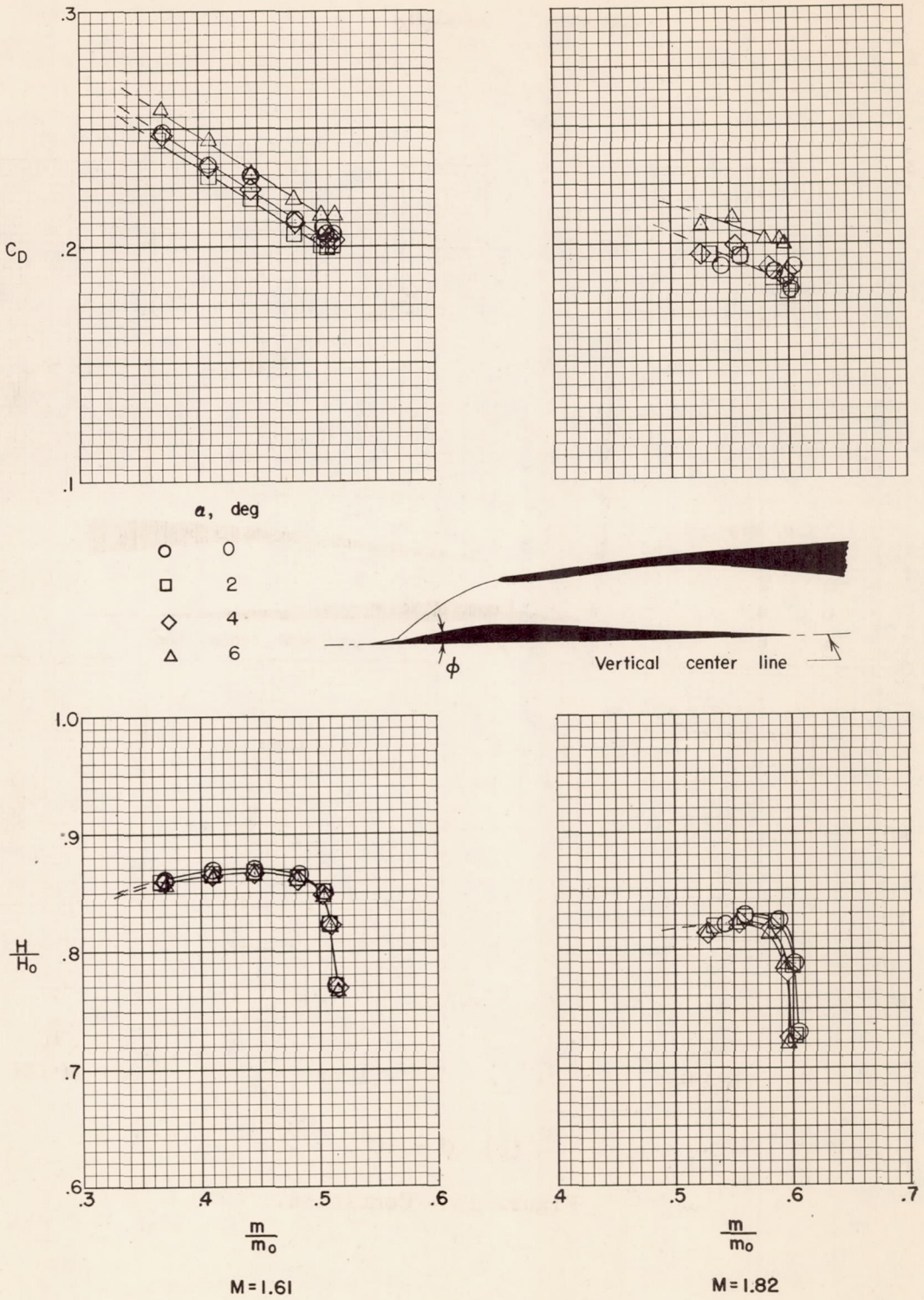

(d) $\phi = 14^{\circ}$.

Figure 15.- Concluded.

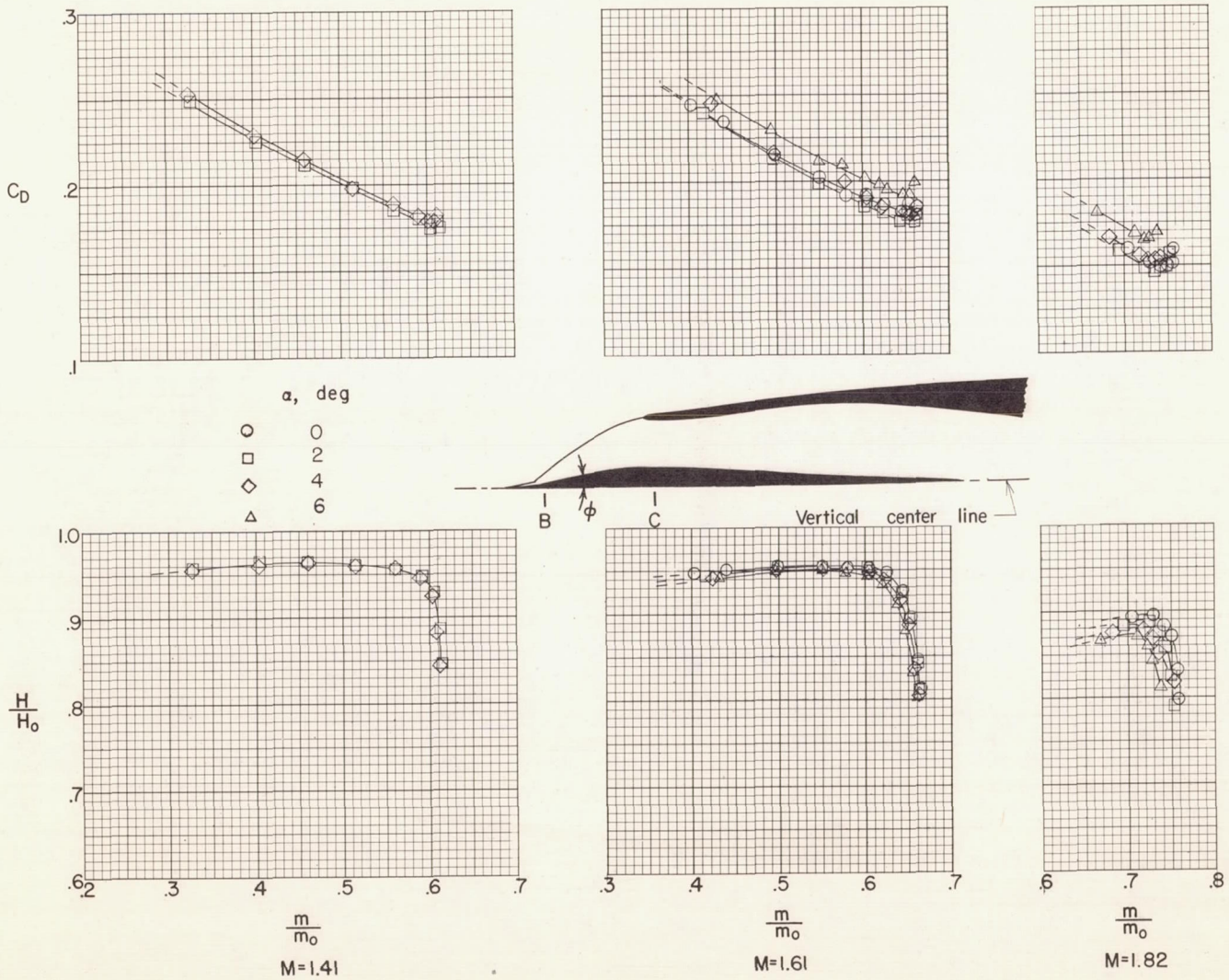

Figure 16.- Pressure-recovery and drag characteristics of inlet B with porous-splitter surfaces (1-BC). h = 0.21 inch; $\phi = 10^{\circ}$.

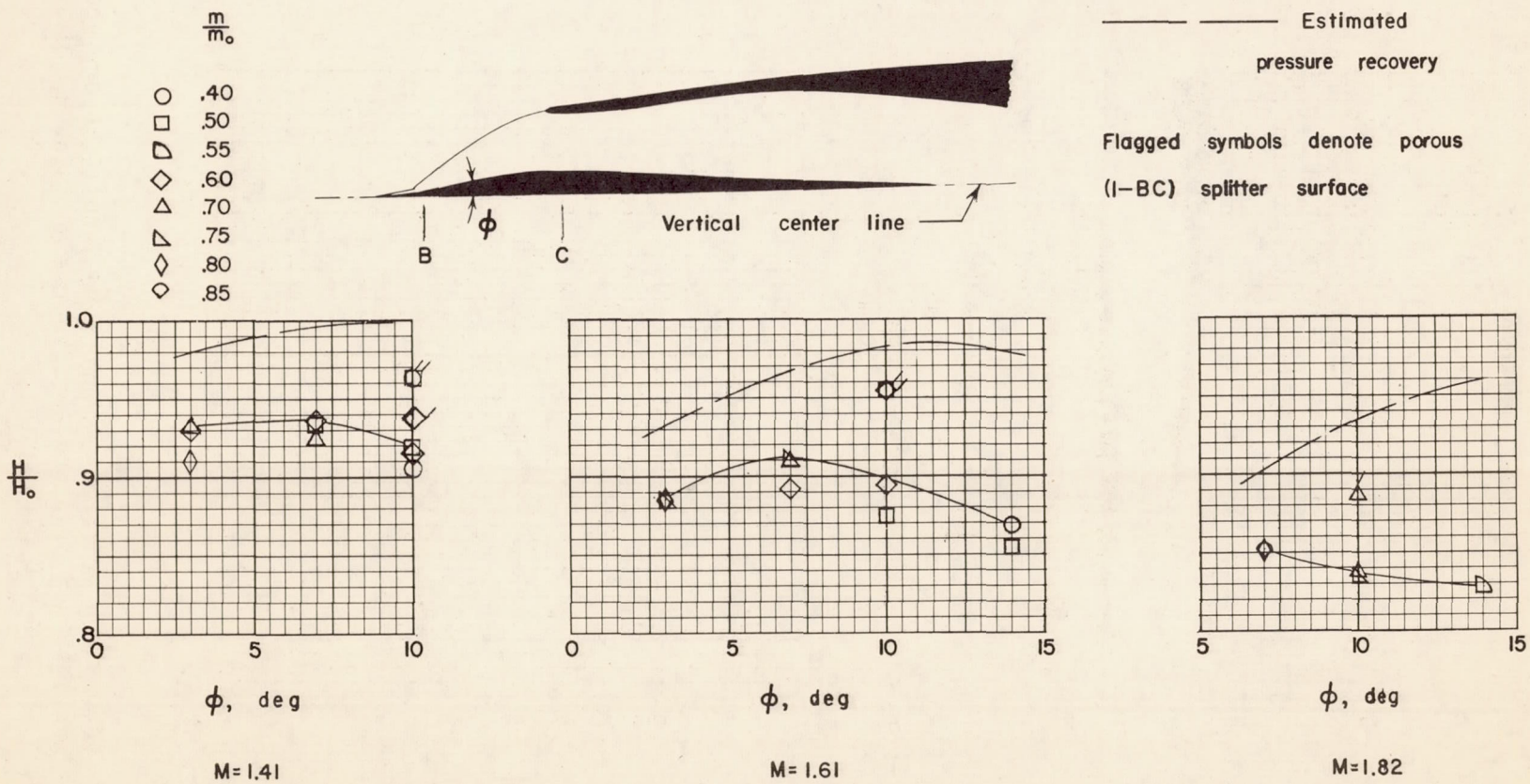

Figure 17.- Variation of pressure recovery of inlet B with splitter half-angle. $h = 0.21$ inch; $\alpha = 2^{\circ}$.

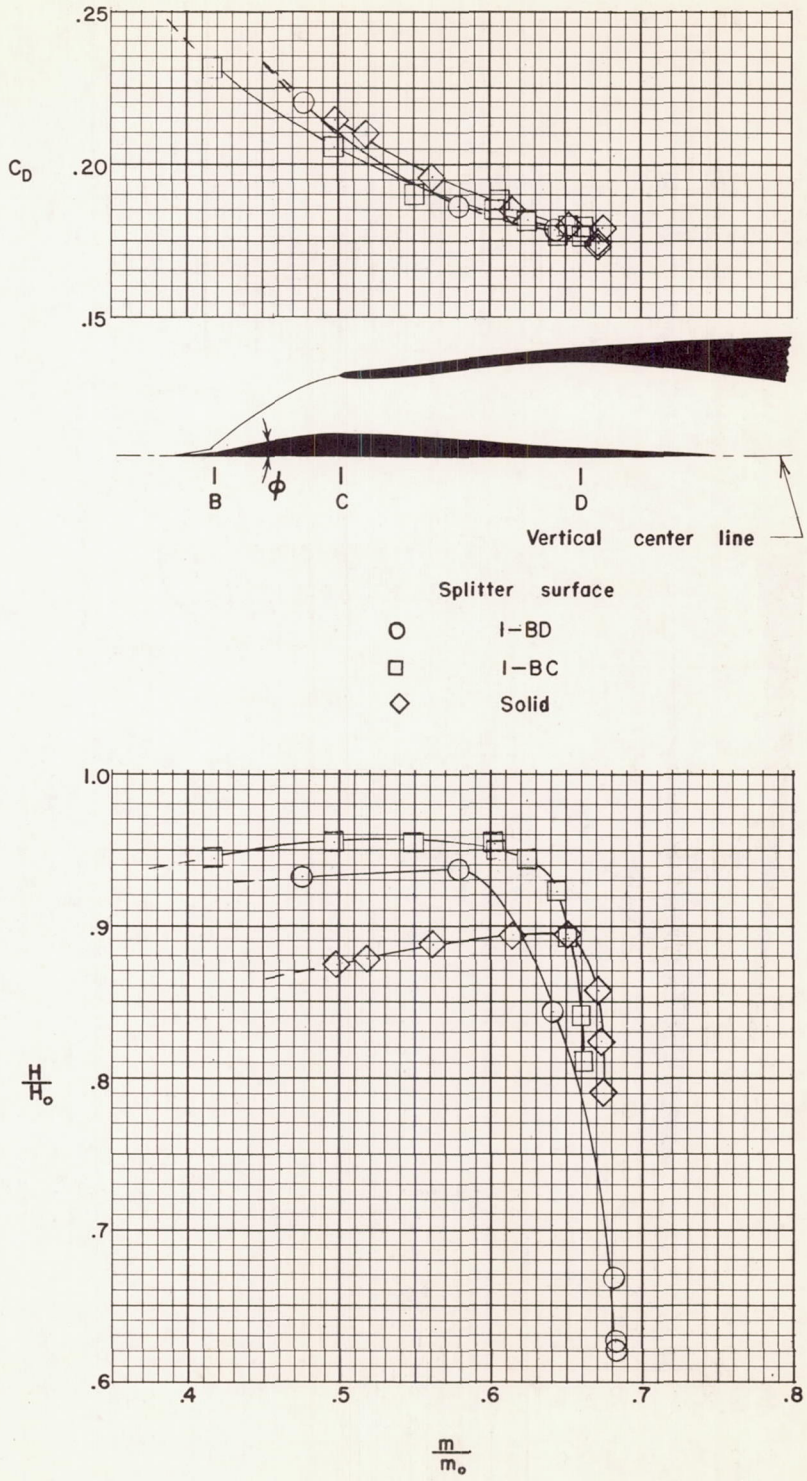

Figure 18.- Comparison of effect of two porous-splitter surfaces on pressure recovery and drag characteristics of inlet B. M = 1.61; $\phi = 10^{\circ}$; $\alpha = 2^{\circ}$; h = 0.21 inch.

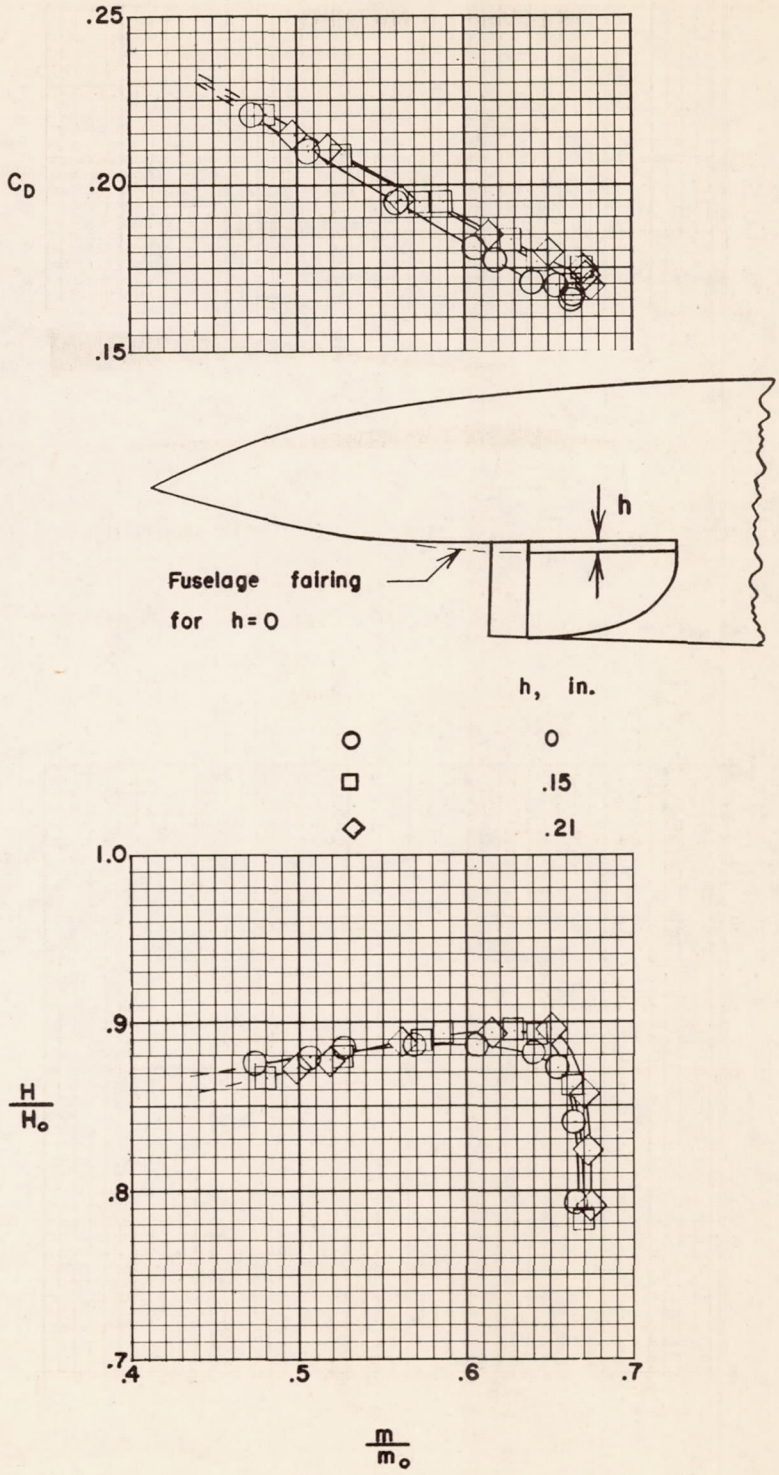

Figure 19.- Effect of boundary-layer bleed height on pressure-recovery and drag characteristics of inlet B without porous-splitter surfaces. $M = 1.61$; $\phi = 10^{\circ}$; $\alpha = 2^{\circ}$.

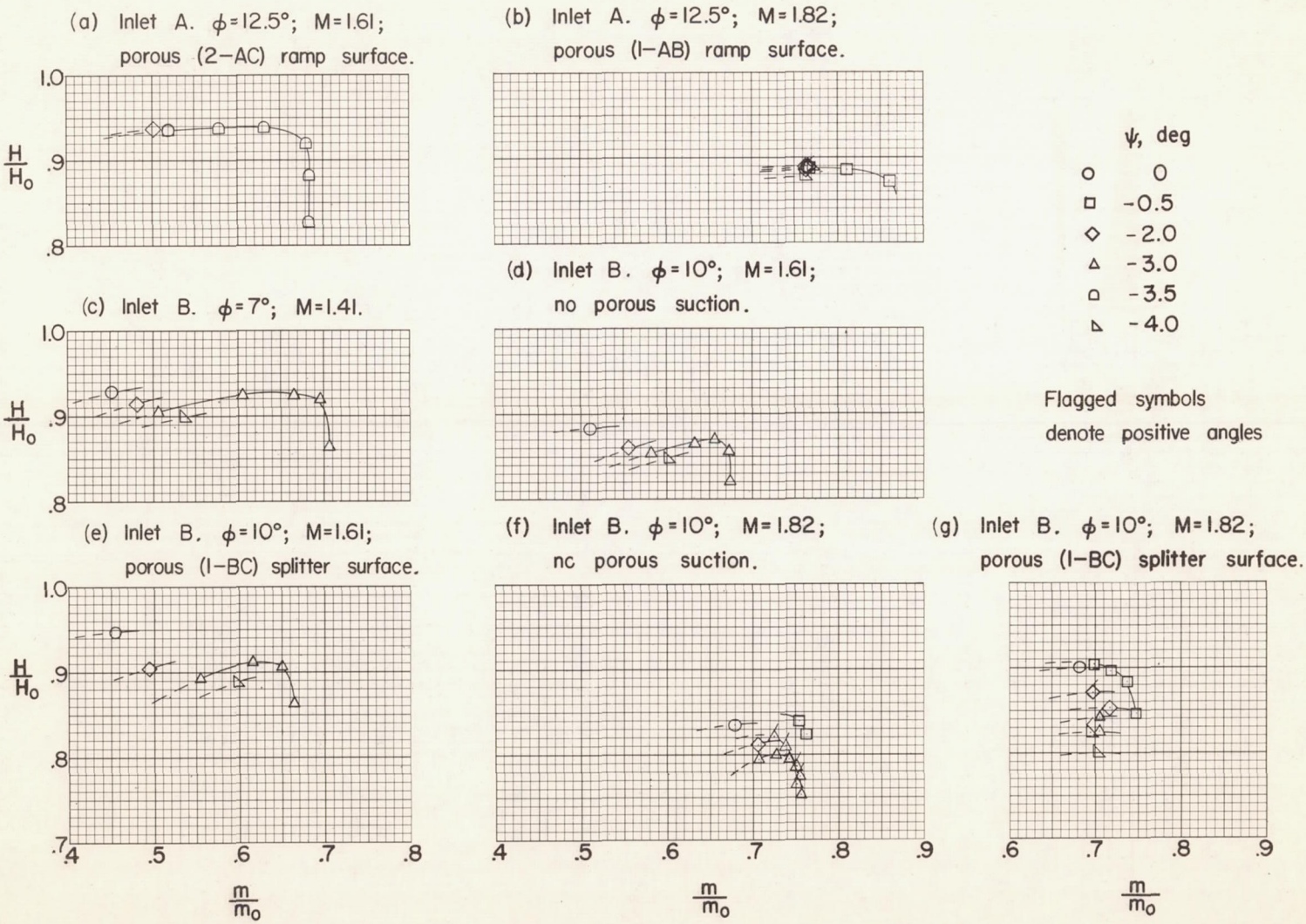

Figure 20.- Effect of yaw on buzz characteristics of inlets A and B. $\alpha = 2^{\circ}$.

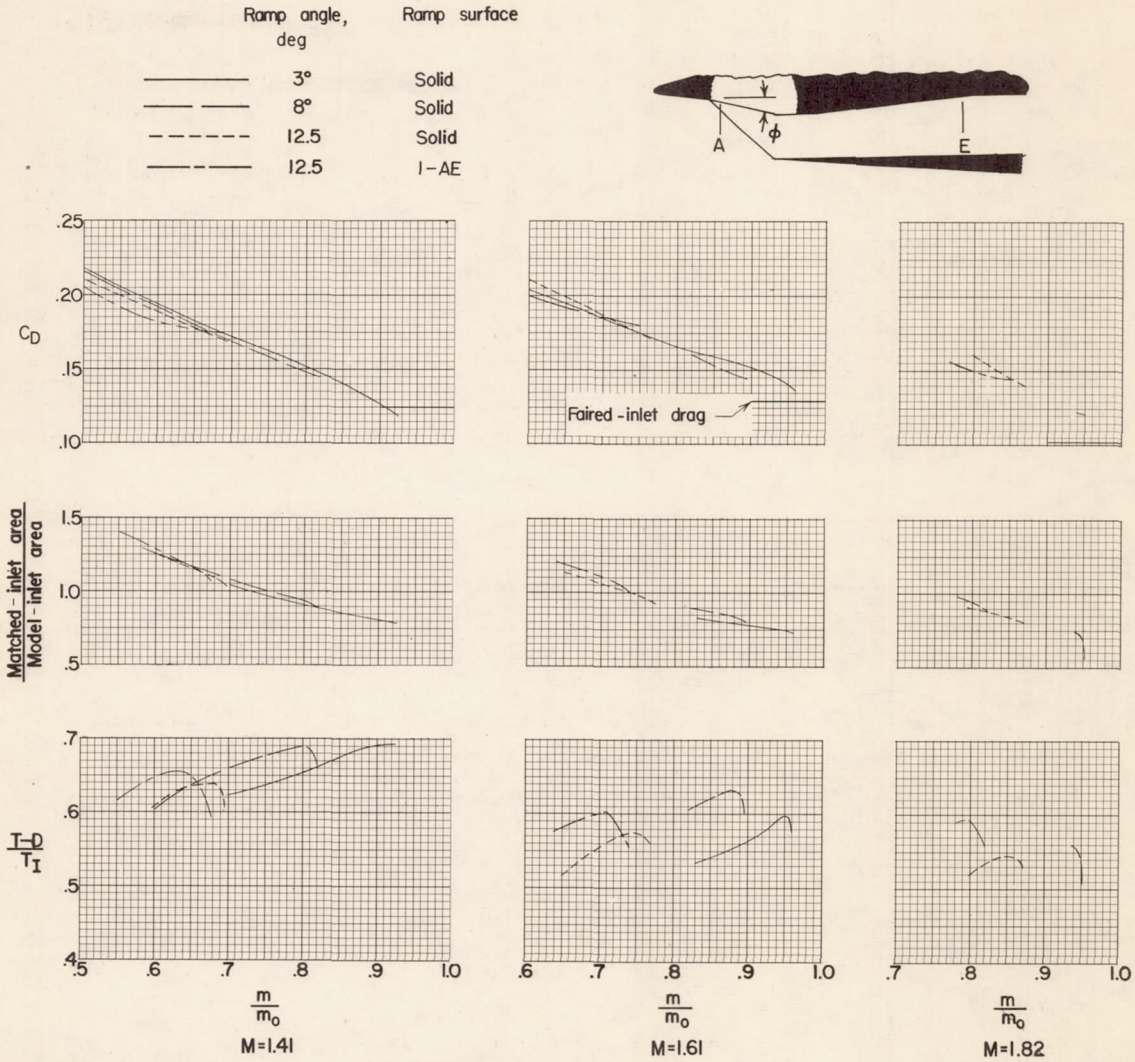

Figure 21.- Variation of drag and thrust-minus-drag characteristics for inlet A. $\alpha = 2^{\circ}$.

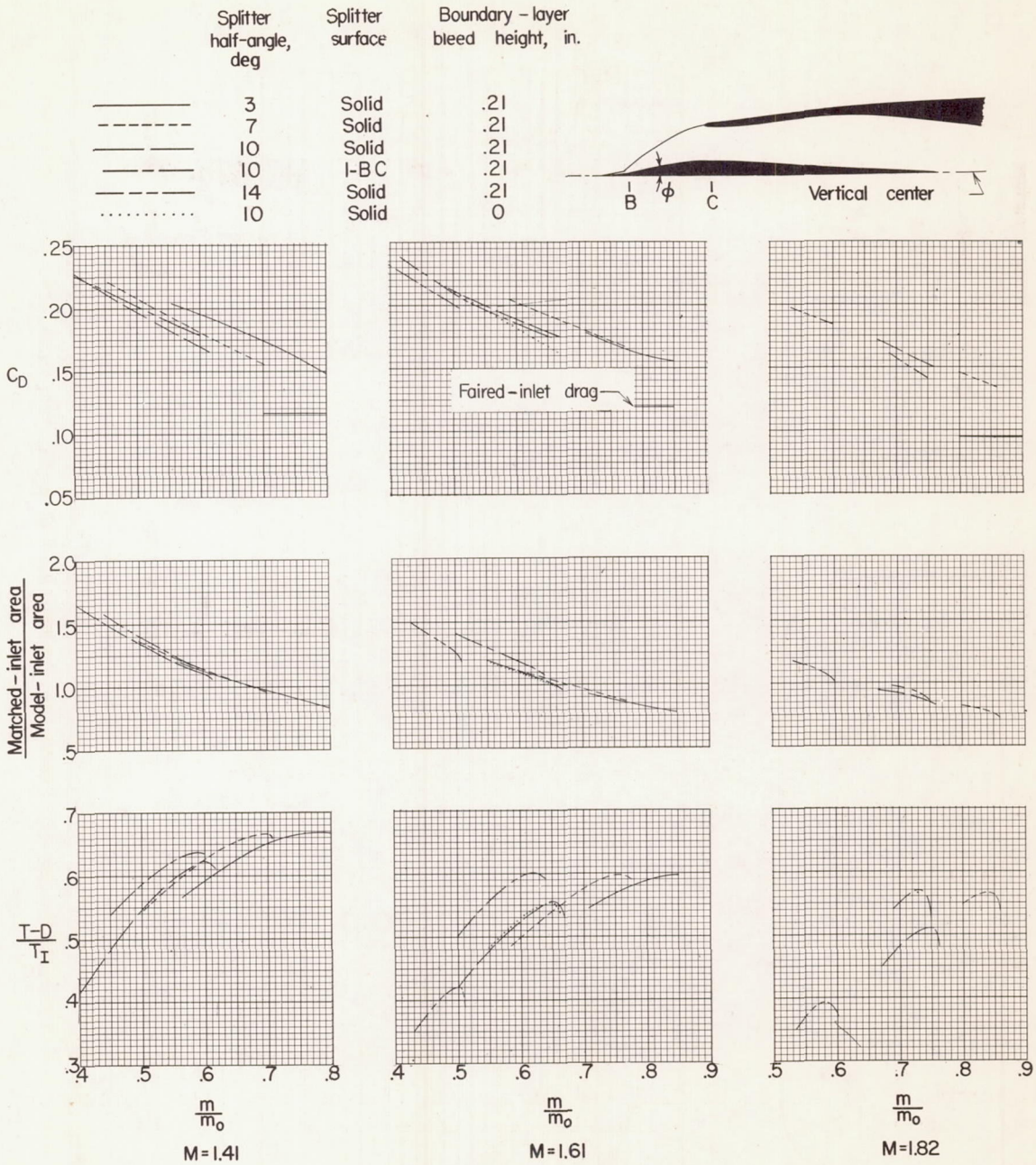

Figure 22.- Variation of drag and thrust-minus-drag characteristics for inlet B. $\alpha = 2^{\circ}$.

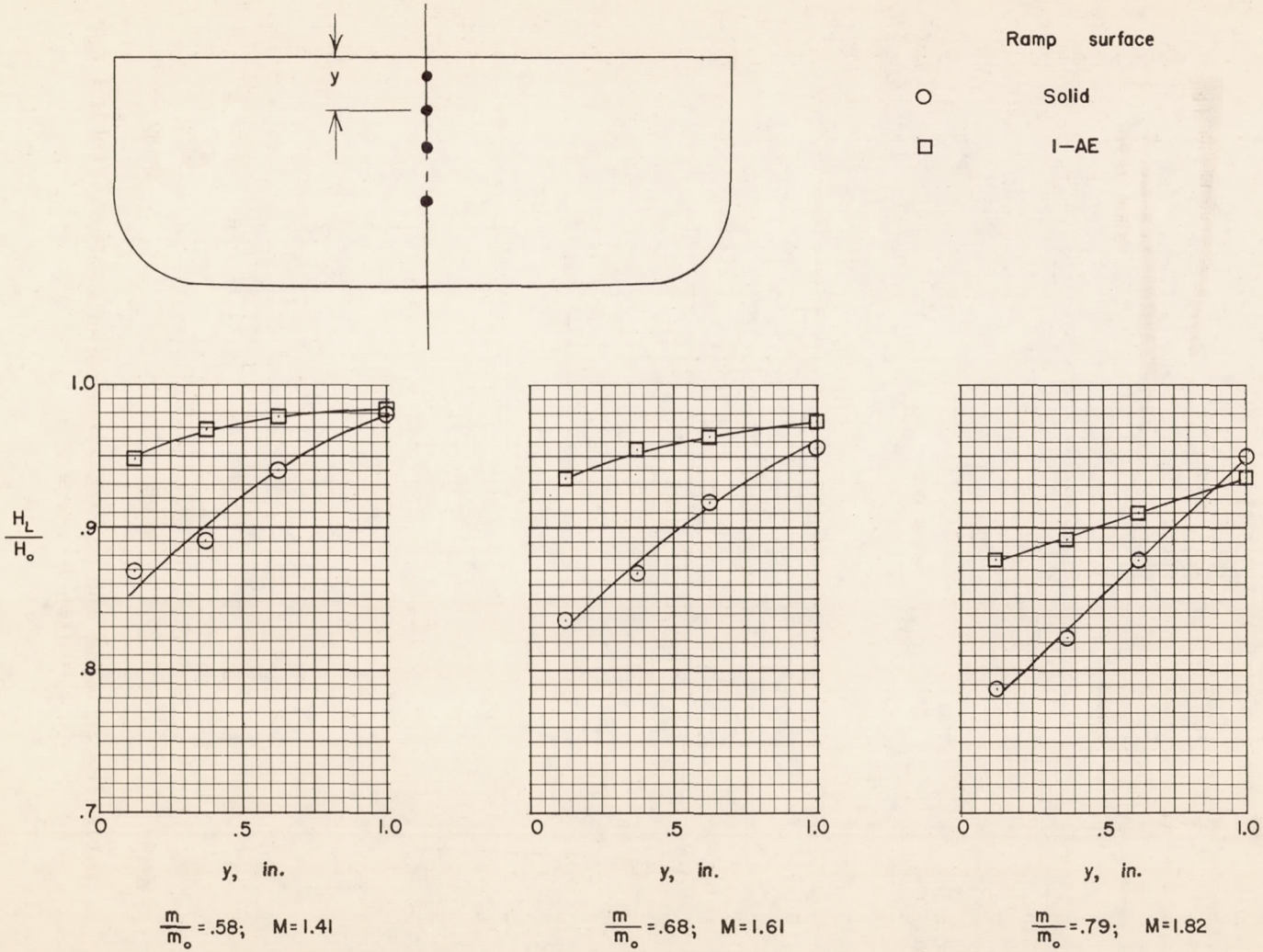

Figure 23.- Effect of porous-ramp surface (1-AE) on total-pressure distribution in diffuser of inlet A. $\phi = 12.5^{\circ}$; $\alpha = 2^{\circ}$.

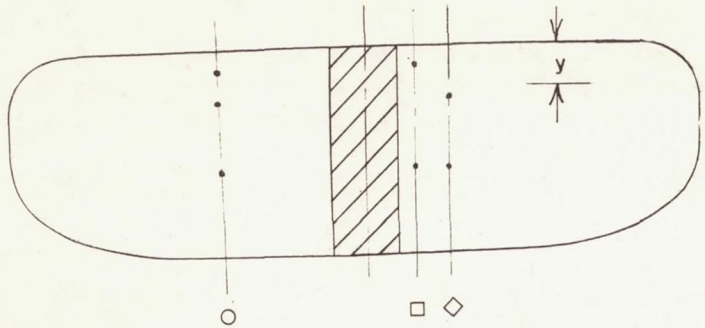

Flagged symbols denote porous – splitter (1–BC) data

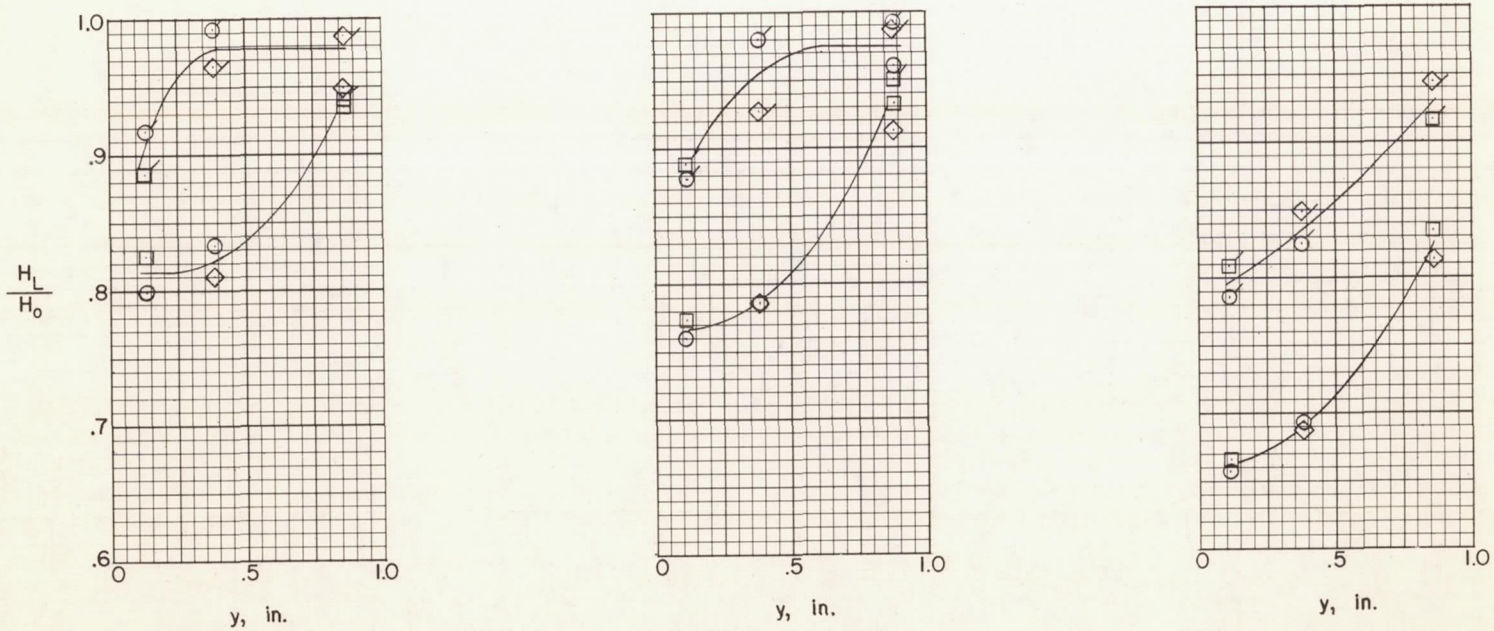

$\frac{m}{m_o}$ = .56; M=1.41

$\frac{m}{m_o}$ = .61; M=1.61

$\frac{m}{m_o}$ = .73; M=1.82

Figure 24.- Effect of porous-splitter surfaces (1-BC) on total-pressure distribution in diffuser of inlet B. $\phi = 10^{\circ}$; $\alpha = 2^{\circ}$.

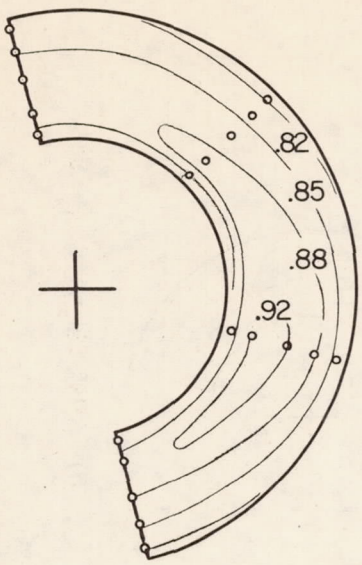

(a) $\phi = 3°$. $\frac{m}{m_o} = .951$; $\frac{H}{H_o} = .869$.

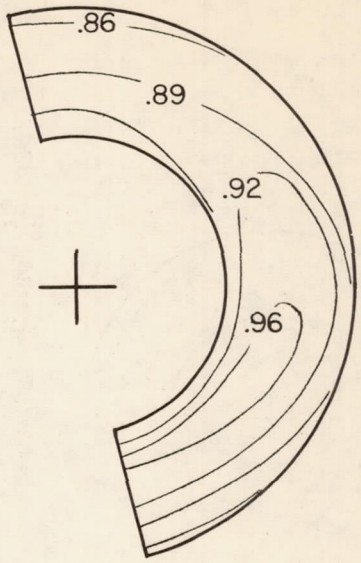

(b) $\phi = 8°$. $\frac{m}{m_o} = .854$; $\frac{H}{H_o} = .909$.

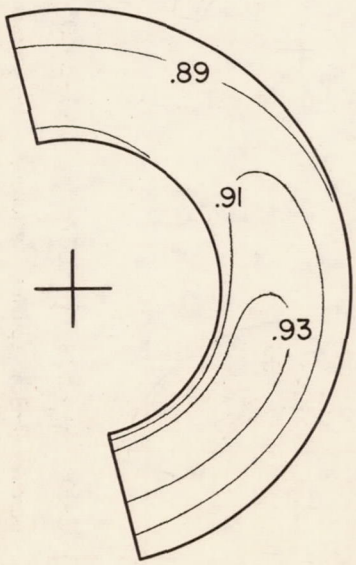

(c) $\phi = 12.5°$. $\frac{m}{m_o} = .713$; $\frac{H}{H_o} = .910$; no porous suction.

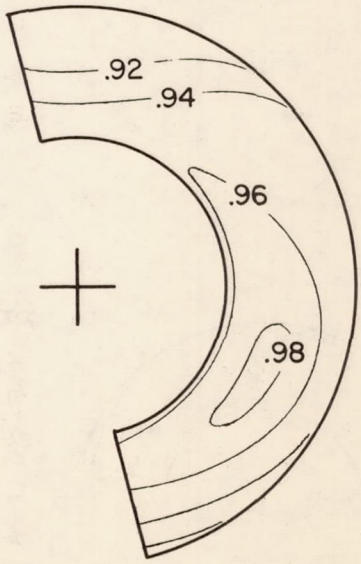

(d) $\phi = 12.5°$. $\frac{m}{m_o} = .679$; $\frac{H}{H_o} = .951$; porous (I-AE) ramp surface.

Figure 25.- Typical total-pressure distributions at compressor face of inlet A. $M = 1.61$; $\alpha = 2^{\circ}$.

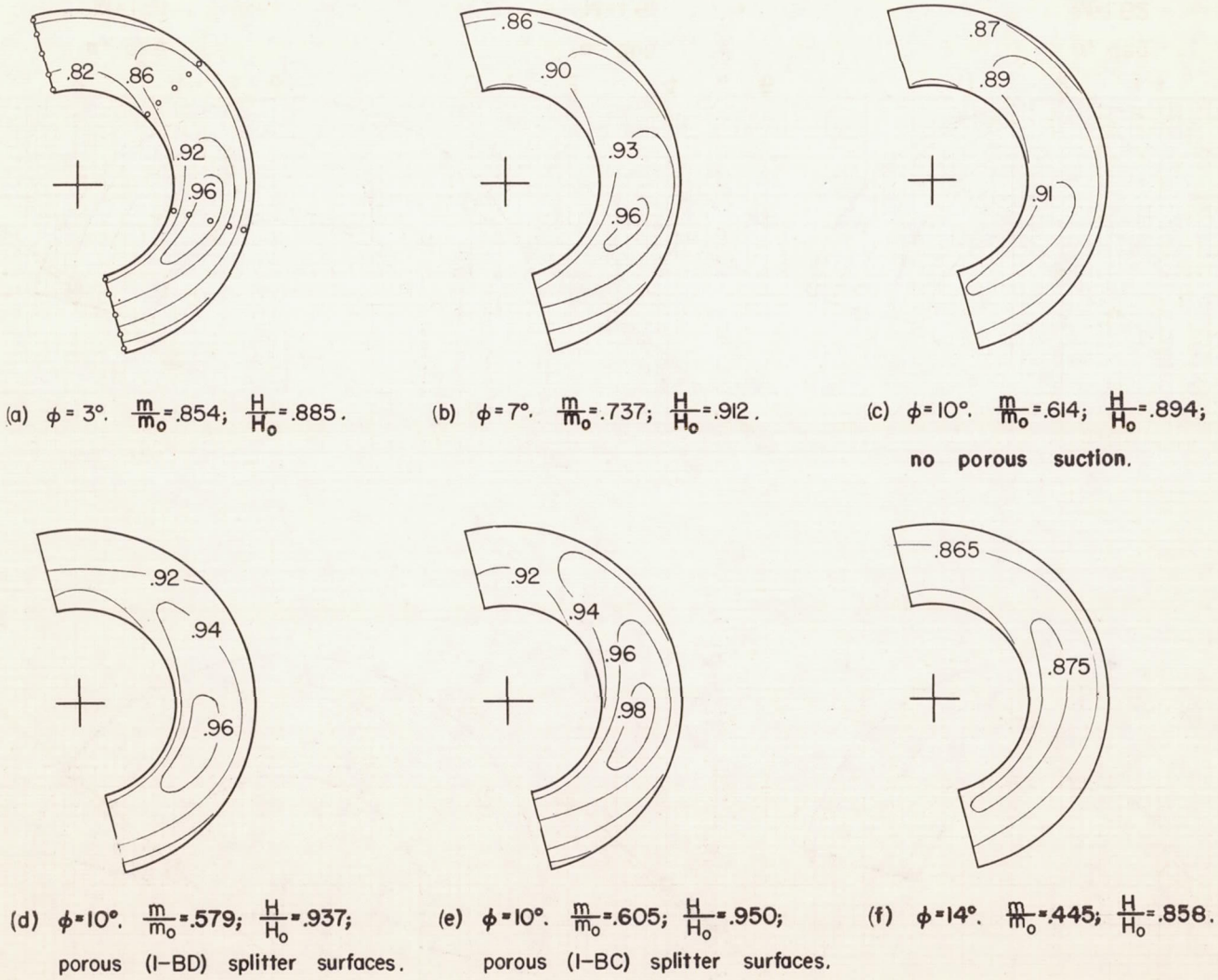

(a) $\phi = 3°$. $\frac{m}{m_o} = .854$; $\frac{H}{H_o} = .885$.

(b) $\phi = 7°$. $\frac{m}{m_o} = .737$; $\frac{H}{H_o} = .912$.

(c) $\phi = 10°$. $\frac{m}{m_o} = .614$; $\frac{H}{H_o} = .894$; no porous suction.

(d) $\phi = 10°$. $\frac{m}{m_o} = .579$; $\frac{H}{H_o} = .937$; porous (I-BD) splitter surfaces.

(e) $\phi = 10°$. $\frac{m}{m_o} = .605$; $\frac{H}{H_o} = .950$; porous (I-BC) splitter surfaces.

(f) $\phi = 14°$. $\frac{m}{m_o} = .445$; $\frac{H}{H_o} = .858$.

Figure 26.- Typical total-pressure distributions at compressor face of inlet B. $M = 1.61$; $\alpha = 2^{\circ}$.

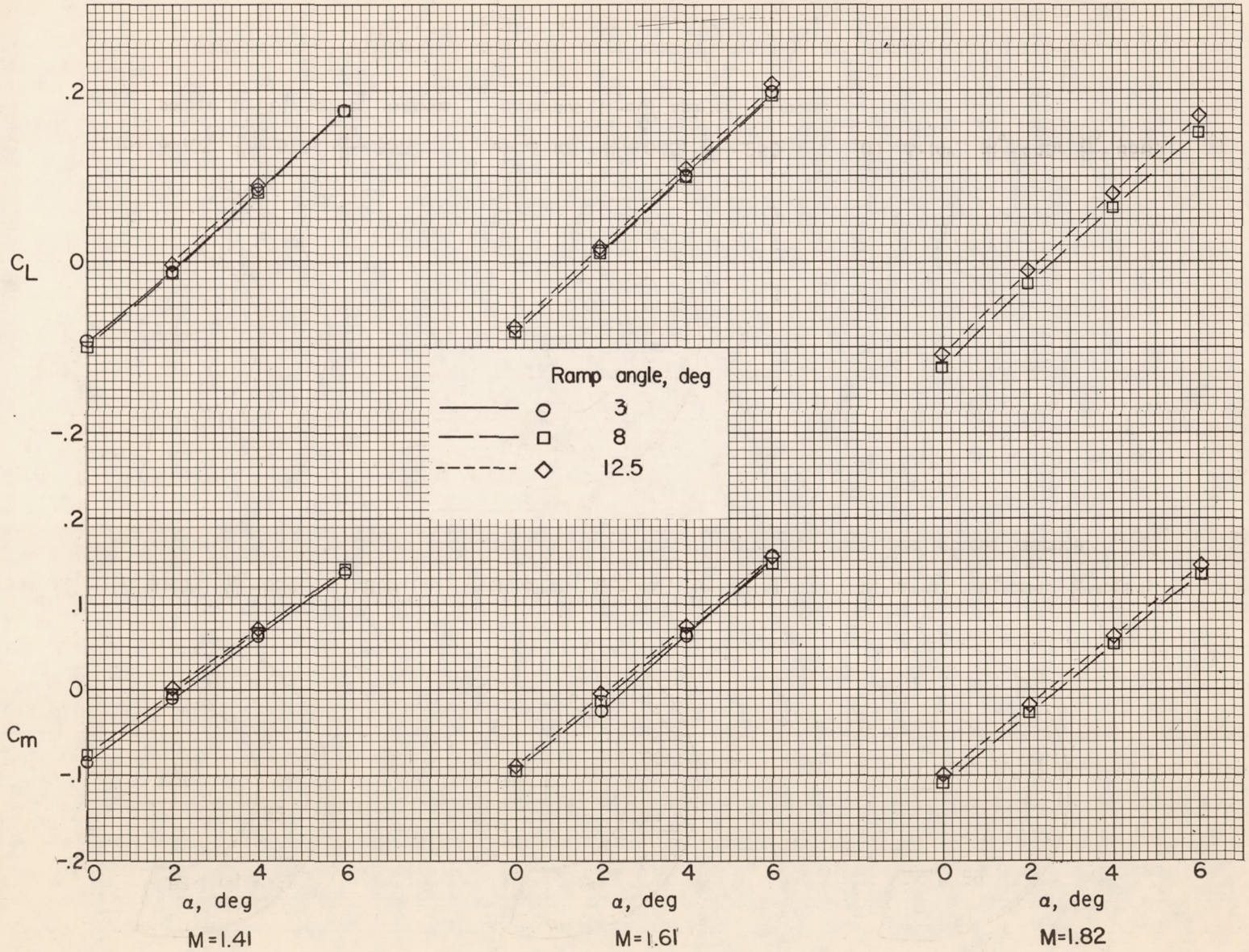

Figure 27.- Lift and pitching-moment characteristics of inlet A.

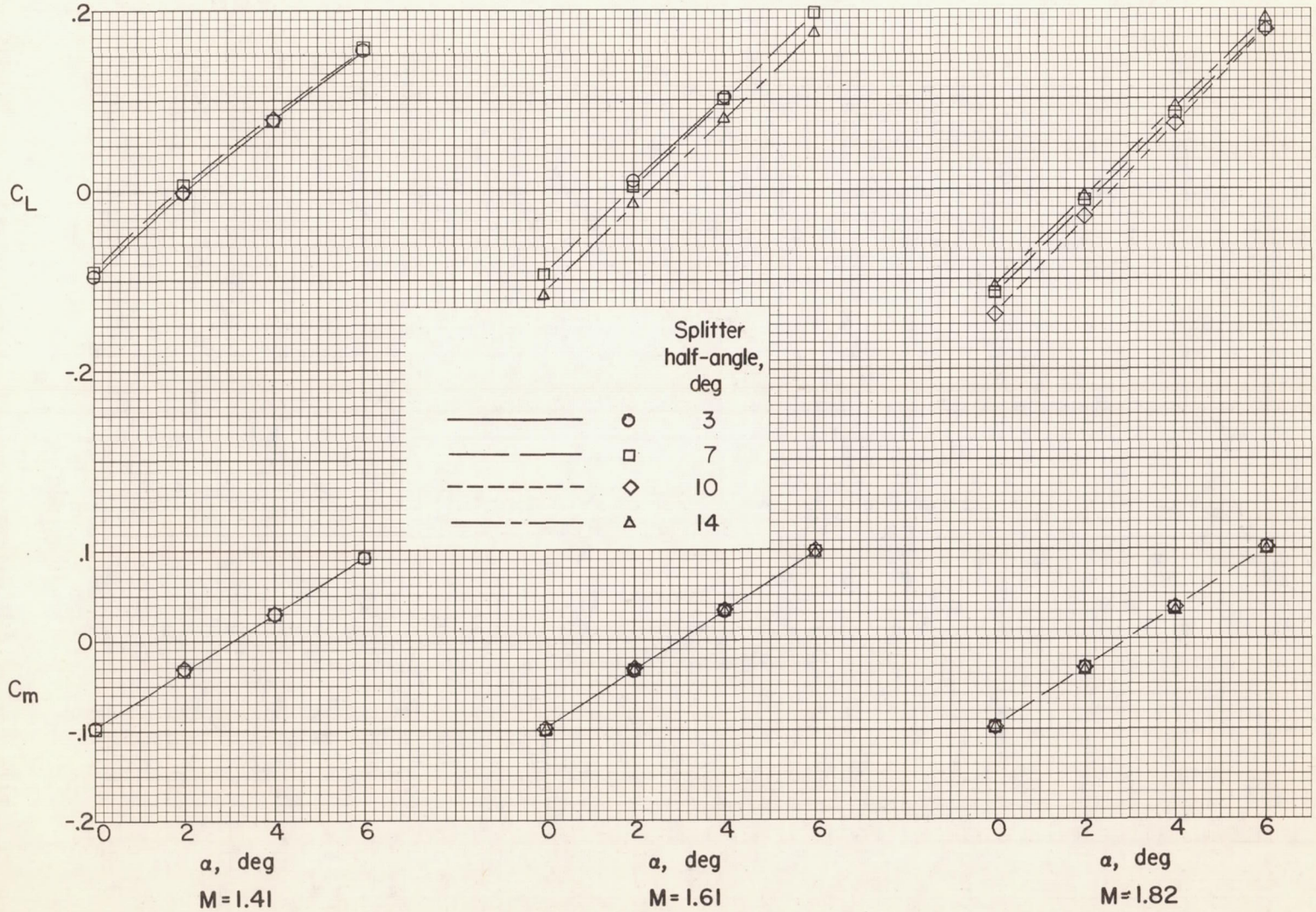

Figure 28.- Lift and pitching-moment characteristics of inlet B.

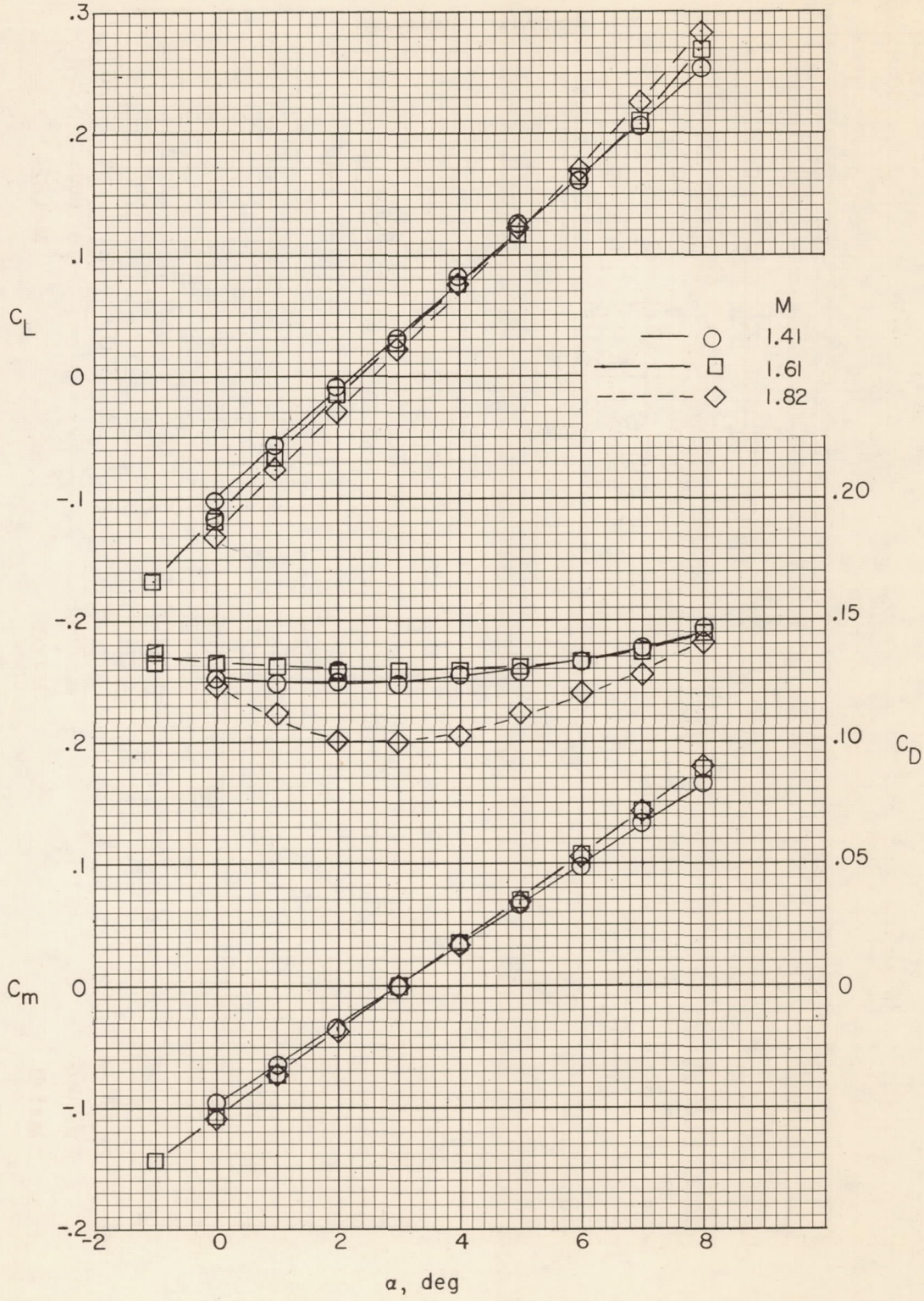

Figure 29.- Lift, drag, and pitching-moment characteristics of faired-nose configuration A.

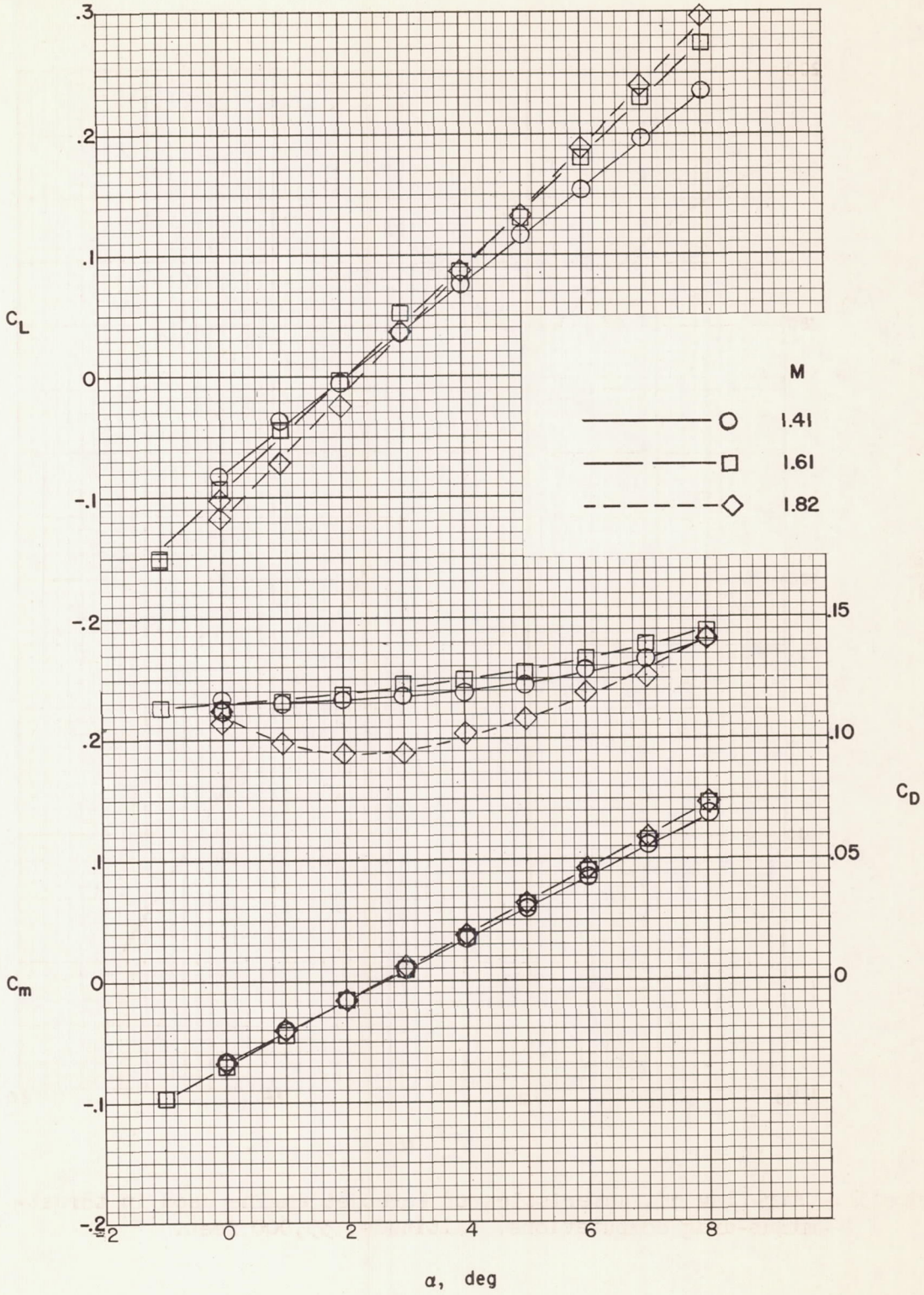

Figure 30.- Lift, drag, and pitching-moment characteristics of faired-nose configuration B.

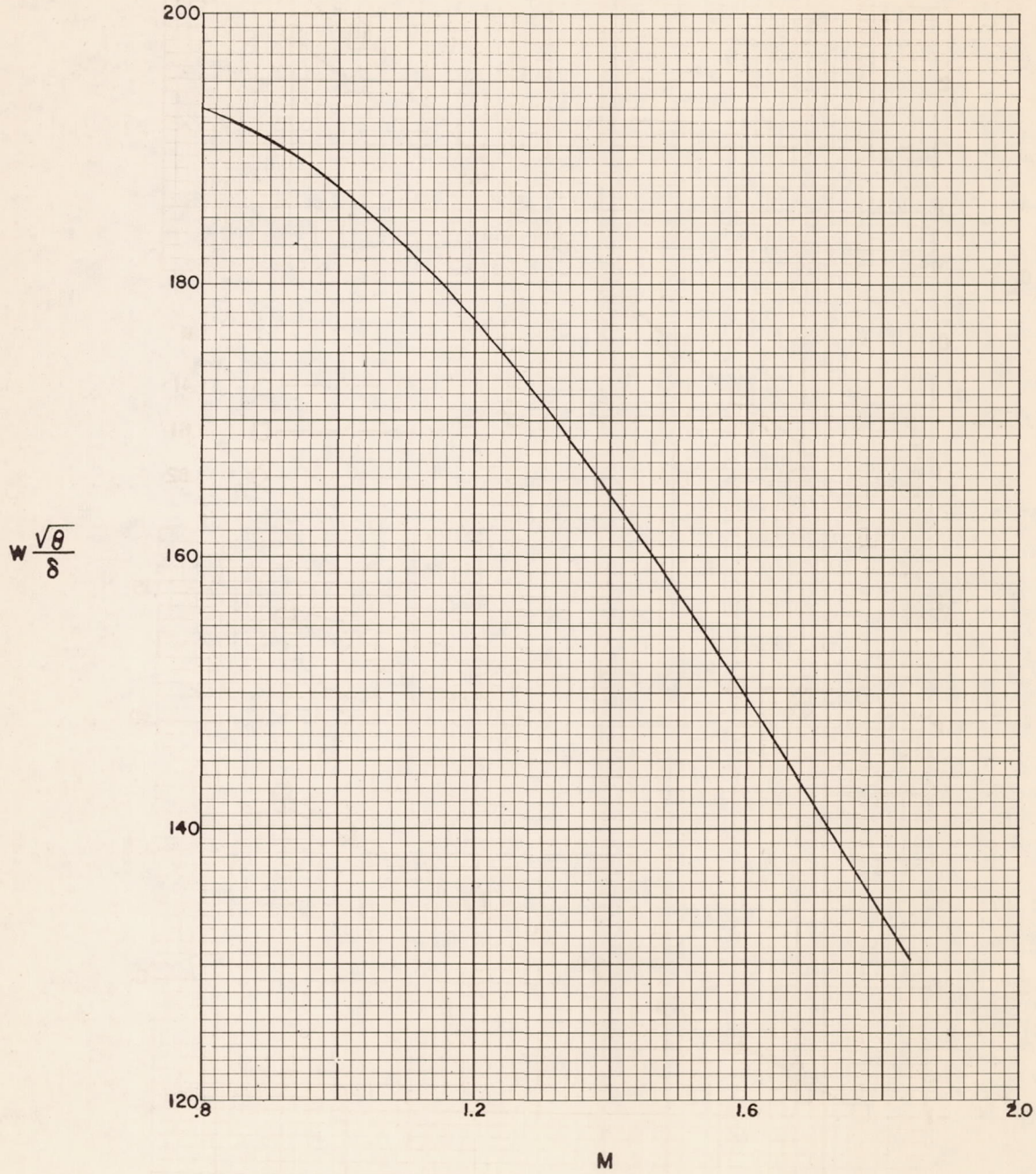

Figure 31.- Air-flow characteristics of turbojet engine used in thrust-minus-drag computations. Altitude, 35,000 feet.